Coupled hydrological and biogeochemical modelling of nitrogen transport in the karst critical zone

Zhicai Zhang [a,c,g], Xi Chen [b,*], Qinbo Cheng [c], Siliang Li [b], Fujun Yue [b,e], Tao Peng [d], Susan Waldron [e], David M Oliver [f], Chris Soulsby [g]

[a] State Key Laboratory of Hydrology-Water Resources and Hydraulic Engineering, Hohai University, Nanjing 210098, China
[b] Institute of Surface-Earth System Science, Tianjin University, Tianjin 300072, China
[c] College of Hydrology and Water Resources, Hohai University, Nanjing 210098, China
[d] Institute of Geochemistry Chinese Academy of Sciences, Guiyang 550081, China
[e] School of Geographical and Earth Sciences, University of Glasgow, Glasgow G12 8QQ, United Kingdom
[f] Biological & Environmental Sciences, Faculty of Natural Sciences, University of Stirling, Stirling FK9 4LA, United Kingdom
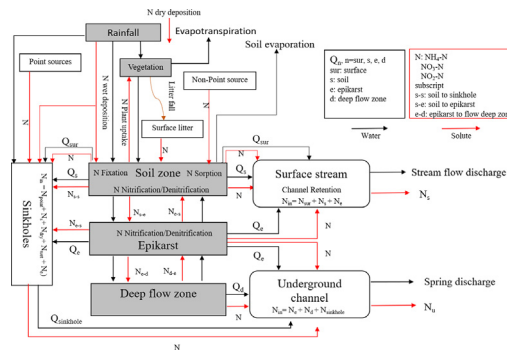[g] School of Geosciences, University of Aberdeen, Aberdeen AB24 3UF, United Kingdom

HIGHLIGHTS

- A novel distributed water-N model for karst catchment was developed.
- Tracer-aided model can significantly reduce equifinality effect of parameters.
- About 45% of N in surface stream and underground channel from epikarst
- Sinkholes are important transport and export pathway of N in karst catchment.

GRAPHICAL ABSTRACT

Distributed hydrological-nitrogen model in karst critical zone.

ARTICLE INFO

ABSTRACT

Transport of nitrogen (N) in karst areas is more complex than in non-karst areas due to marked heterogeneity of hydrodynamic behaviour in the karst critical zone. Here, we present a novel, distributed, coupled hydrological-biogeochemical model that can simulate water and nitrogen transport in the critical zone of karst catchments. This new model was calibrated using integrated hydrometric, water stable isotope, and nitrogen-N concentration data at the outflow of Houzhai catchment in Guizhou province of Southwest China. Hydrological dynamics appears to control N load from the study catchment. Combining flow discharge and water stable isotopes significantly constrained model parameterisation and mitigate the equifinality effects of parameters on the simulated results. Karst geomorphology and land use have functional effects on spatiotemporal variations of hydrological processes and nitrogen transport. In the study catchment, agricultural fertilizer was the largest input source of N, accounting for 86% of the total. Plant uptake consumed about 45% of inputs, primarily in the low-lying valley bottom areas and the plain covered by relatively thick soils. Thus, a large amount of N released from soil reservoirs to the epikarst (via fractures or sinkholes) is then exported to the underground channel in the limestone area to the south. This N draining into groundwater could lead to extensive, potentially long-

* Corresponding author.
    E-mail address: xi_chen@tju.edu.cn (X. Chen).

term contamination of the karst system. Therefore, improving the efficiency of fertilization and agricultural management in valleys/depressions is an urgent need to reduce N losses and contamination risk.

1. Introduction

Carbonate bedrock is a significant continental surface, comprising ~12% of ice-free land and providing water resources for about 25% of the Earth's population (Ford and Williams, 1989). The southwest China karst region is one of the largest globally continuous karst areas, covering ~540 × 10³ km² over eight provinces. Agro-forestry and mineral extraction dominate land use, with subsistence-agriculture where soils exist (terraced gentler hillslopes/valley floors), and forest in uncultivated steeper mountains. From ~1950–1980 deforestation for creating cultivation space caused accelerated soil erosion, a changed hydrological balance and, shaped by agricultural practices, poorer water quality. Anthropogenic N fluxes have also been increasing as a result of population growth, agricultural intensification, fossil fuel-related acid deposition in industrialised- and agriculturally-intensified regions. Moreover, significant soil percolation and subsequent rapid preferential flow in the critical zone provides limited buffering for contaminant attenuation before re-emergence. It is therefore important to understand what controls water quality, and the source and attenuation of contaminants in this sensitive landscape. Models can help understanding of how nitrogen is cycled and transported and the key factors and processes that control its dynamics. Modelling results provide quantitative estimates of how a system will respond to changes in pollutant inputs to aid environmental management (Ranzini et al., 2007).

The transfers of N in karst areas are more complex than those in non-karst areas because of the marked spatial heterogeneity of hydrodynamic behaviour. Lumped parameter models conceptualising reservoirs of the critical zone in series and/or parallel have been popularly used to simulate flow and nitrate movements and its biogeochemical reaction in karst areas (Husic et al., 2019). However, these lumped models lack functionality in relation to the spatial heterogeneity of hydrological-N processes characterising karst landforms, geology and land cover. Distributed hydrological-nutrient models, like SWAT (Arnold et al., 1998), have been widely used to simulate hydrological and nutrient responses to changes of land surface conditions. Expanding the grid-pattern hydrological model functions using process-oriented biogeochemical modules, such as the DeNitrification-DeComposition (DNDC) module (Li et al., 2000), facilitates comprehensive simulation of nitrogen transformation, vertical movement of water and nitrogen in soils and effluxes of carbon and nitrogen gases (Ferrant et al., 2011; Zhang et al., 2016, 2017a; Zhang et al., 2018). However, these models are developed for matrix flow systems therefore cannot be directly applied in karst areas. In karst areas, the high permeability of rock fractures leads to considerable changes in water storage and water age by facilitating mixing of new and old water during rainfall events (Zhang et al., 2019). Channelled flow in sub-surface conduits also exchanges reversibly with small fractures in the surrounding matrix depending on the hydraulic gradient between them (Hartmann et al., 2014). Sinkholes are special features in karst areas, which receive both diffused and concentrated autogenic recharge, and then drain through a shaft or an underlying solution conduit (Tihansky, 1999). Therefore, over different, linked porous media, biogeochemical processing capacities can vary drastically (Jones and Smart, 2005; Opsahl et al., 2017; Yue et al., 2015). Until now, only a few models can appropriately delineate the unique hydrological-nitrogen cycle of karst systems.

A particular challenge in coupled hydrological-biogeochemical modelling is the increased risk of equifinality as model parameters increase (Zhang et al., 2016; Zhang and Shao, 2018). However, recently using tracer-aided models has helped ensure robust hydrological modules in coupled models. Using water stable isotopes or other tracers (e.g.

chloride) in calibration, in addition to the more commonly used target of flow, can help constrain parameterisation at the catchment scale while giving increased confidence of accurate process representation of runoff sources (Birkel et al., 2015). Tracer-aided models can also strengthen conceptualisation of hydrological functions and transport of water particles, in terms of water age, dominant flow paths and hydrological connectivity in different model compartments. Such quantitative hydrological understanding can be functionally linked to solute transport in water quality models (McDonnell and Beven, 2014; Sprenger et al., 2015). These advantages of stable isotopes have been successfully exploited in enhancing the reliability of modelling dominant hydrological processes in non-karst catchments (Soulsby et al., 2015; Piovano et al., 2018) - but the efficiency of the tracer-aided functions applied in the hydrological-biogeochemical model in karst catchments is unknown.

Our previous work in the Chenqi catchment, a sub-catchment of the Houzhai catchment, Guizhou province of Southwest China, has focused on a typical karst landscape and associated karst critical zone architecture (Vertically, the earth critical zone refers to a permeable layer from the tops of the trees to the bottom of the groundwater. Here, karst critical zone encompasses vegetation, soils, epikarst and deep aquifer.). In this prior work, we developed a distributed hydrological model (Zhang et al., 2011). In this study, we extend this model to facilitate multi-criteria calibration based on detailed observations of water stable isotope composition; we also couple biogeochemical modules to the hydrological structure to simulate spatially spatially-distributed fluxes of N, and apply the model to the larger Houzhai catchment. We address the three questions: (1) How do interacting karst geomorphological features, such as fractures and conduits, sinkholes, and surface streams and subsurface channel, control hydrological-nitrogen processes? (2) How effective is the tracer-aided model in reducing modelling uncertainty? (3) How much N in the catchment N budget is contributed from different sources in the critical zone and from different land uses?

2. Study area and data

2.1. Study area and descriptions of critical zone structure

2.1.1. Study area

The Houzhai catchment, located in Puding County, Guizhou Province of southwest China, has an area of 73.5 km² (Fig. 1). The site has a subtropical wet monsoon climate. The mean annual temperature is 20.1 °C. The highest monthly average temperature is in July, and the lowest is in January. Annual precipitation is 920 mm, with a distinct summer wet season and a winter dry season. Monthly average humidity ranges from 74% to 78%. The lithology is ~90% Triassic argillaceous limestone and dolomite. The elevation of the study area varies from 1218 to 1565 m above sea level, high in the east and low in the west (Fig. 1). The karst topography in this catchment includes many exposed funnels and sinkholes and a well-developed underground channel network. Buried karst is located in the valleys and poljes, which are surrounded by karst mountainous peaks. The east mountainous area has the typical cone and cockpit karstic geomorphology of southwest China. The cone peaks are generally 200–300 m above the adjacent sinkhole depressions while the cone surface relief and slope are much steeper.

2.1.2. Vegetation and soils

The land use and cover in the catchment include forests (mostly a mix of trees and shrubs), cultivated fields, villages and open water
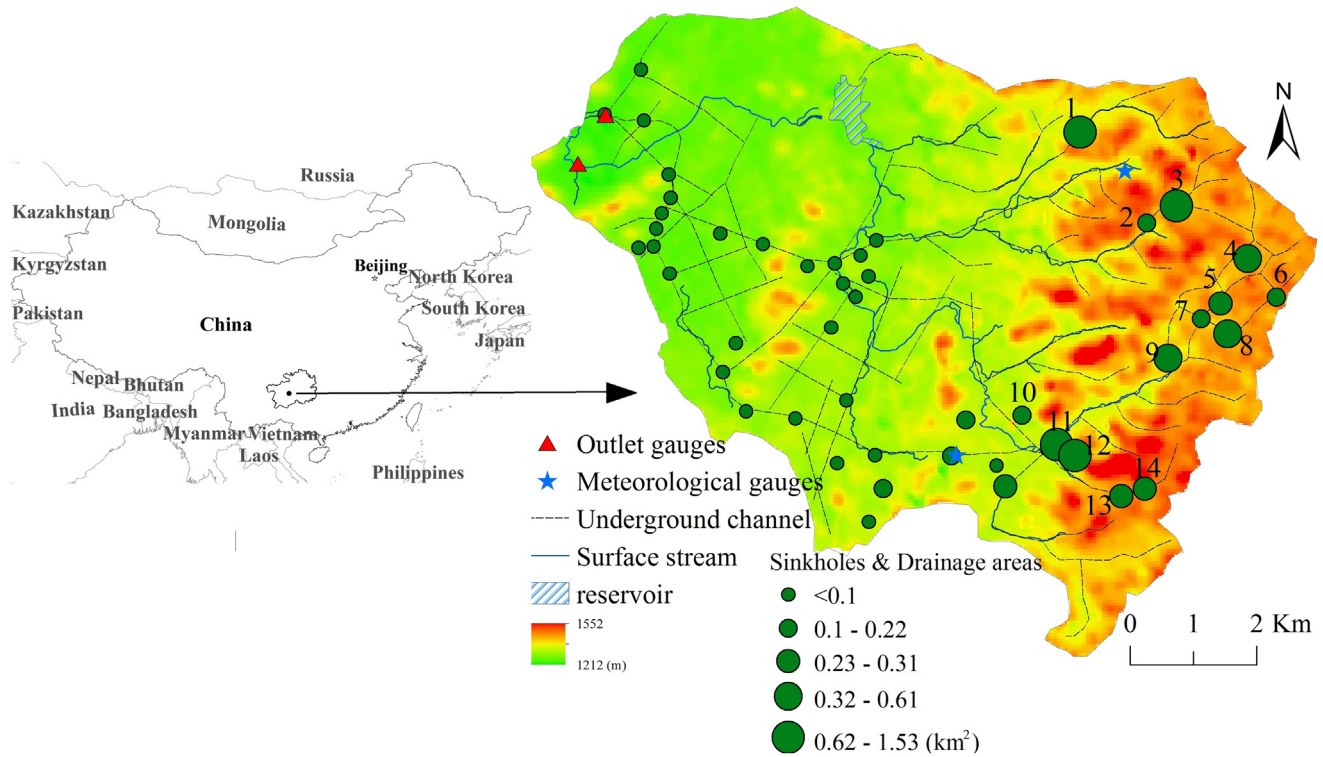
Fig. 1. Topography, surface stream and underground channel network, and sinkhole location in Houzhai watershed. The size of dots represents the drainage area controlled by sinkholes and the black number represents the sinkholes in the eastern mountainous area.

(Fig. 2a). The soils are classified as limestone soil, paddy soil, and yellow soil (Fig. 2b). Field investigations of soil thickness and hydraulic properties have been undertaken. The soil thickness ranges 0–2.0 m, increasing from steep hillslope (0–50 cm) to gentle plain areas (1–2 m).

2.1.3. Epikarst

Below soils or at the outcropping carbonate rocks, the uppermost layer of the rock is referred to as the "epikarst". It develops close to the topographic surface through rapid dissolution (Williams, 2008). Field investigations of a rock profile in the eastern mountainous area (Fig. 2c) showed that the epikarst zone underlying the thin soils is rich in fractures and conduits while density and volume of the fractures generally decrease with increasing depth from ground surface (Zhang et al., 2013). Some infiltrated water can become perched in the epikarst zone as the porosity and permeability below decline markedly (Klimchouk, 2004). The distribution of epikarst thickness across the catchment was investigated at five profiles (Fig. 2c) using GPR (MALA Professional Explorer (ProEx) System) with a RTA 100-MHz antenna frequency and the software of Reflexw. The radargrammes clearly identify the thickness of the weathered zone, for example, the purple colour represents a low propagation velocity of electromagnetic waves in the ground for A and B profiles, and the zone with intensive changes of colour is characterized by strong fractured rocks.

From these profiles and the established relationship between the epikarst thickness and terrain curvatures (Zhang et al., 2012), the epikarst thickness in the entire catchment was interpolated using a digital elevation model (DEM) data derived from the 1:10000 digital topography map in the catchment. The generated depth of epikarst zone ranges from 7 to 28 m (Fig. 2c), shallower in the eastern mountains and deeper in the western plains.

2.1.4. Deep aquifer

The aquifer system consists mainly of limestone and dolomite of the Middle Triassic Guanling Formation (Fig. 2d). The degree of inclination of the strata in this formation is between 5° and 25° to the northwest.

The Middle Triassic Guanling Formation can be divided into T_2g^1, T_2g^2, and T_2g^3 (A-B section in Fig. 2d) from the oldest to the youngest according to the combined characteristics of the lithology (Yang, 2001). The karst fissures and conduits are well developed in the aquifers. In particular, dense conduits can be found in the south limestone area (Yang, 2001). The groundwater depth decreases from >10 m in the east to ~2 m in the west, following the topography (Fig. 3d). The aquifer boundary is similar to the catchment boundary except in the south where <5% of water is lost to a neighbouring catchment through conduits (Yu et al., 1990). The catchment mean recharge coefficient (recharge amount divided by precipitation) is about 0.47 (Yu et al., 1990). A large proportion of the infiltration and percolation comes from direct runoff and sinking streams (allogenic recharge from the surrounding areas) in the rain season. The aquifers mostly are unconfined, however, they are markedly heterogeneous (Yu et al., 1990), with both subsurface flow of low velocity in the matrix (small fissures and fractures) and fast flow velocity in the karst conduits. Consequently, spatio-temporal variability in the water table is extremely high (Chen et al., 2018).

2.1.5. Sinkhole in connection with deep aquifer

Sinkholes usually develop in terrain depression areas (Kruse et al., 2006), which overlie the underground channel. In the study catchment, 47 sinkholes have been identified based on the field investigations (Fig. 1). Based on a DEM, the flow direction tool in ARCGIS is used to create a direction raster that identifies the drainage area of every sinkhole in the study area (Fig. 1). Fourteen sinkholes in the eastern mountainous area are identified with a total area of 8.22 km², which accounts for 11% of the total catchment area. The smallest and largest sinkhole drainage areas are 0.17 and 1.53 km², respectively. The total area of the 33 sinkholes in the western plain area is 1.64 km², which accounts for only 2% of the total catchment area. Therefore, the western sinkholes collect less storm flow compared to the eastern sinkholes (Yu et al., 1990). Additionally, the western sinkholes are mainly produced by the collapse of rocks overlying the underground channel and drain small areas. They take a similar function in receiving storm flow as the
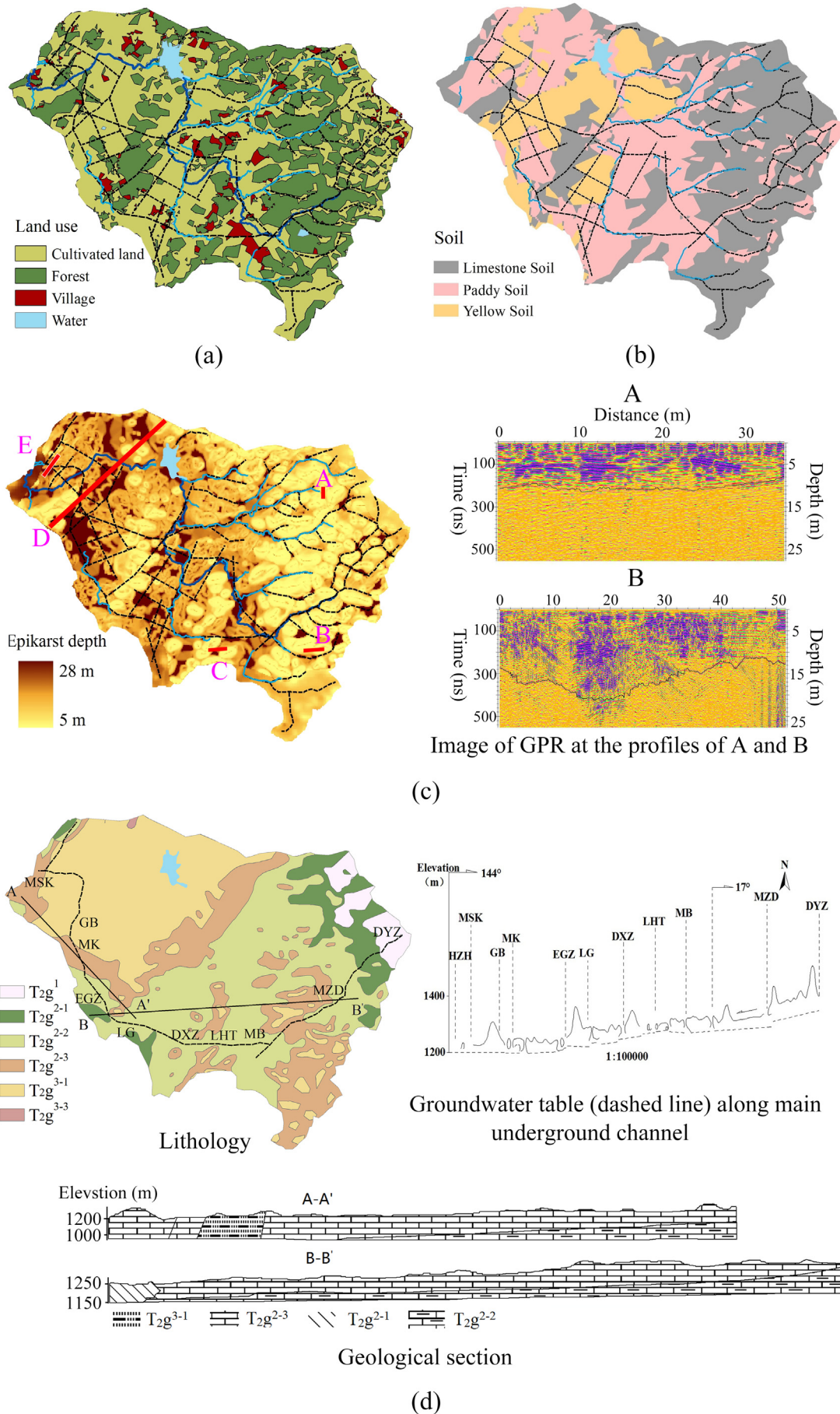
Fig. 2. Distribution of karstic critical zone structure for land use/cover (a), soils (b), epikarst (c), and aquifer geology (d) in Houzhai catchment.
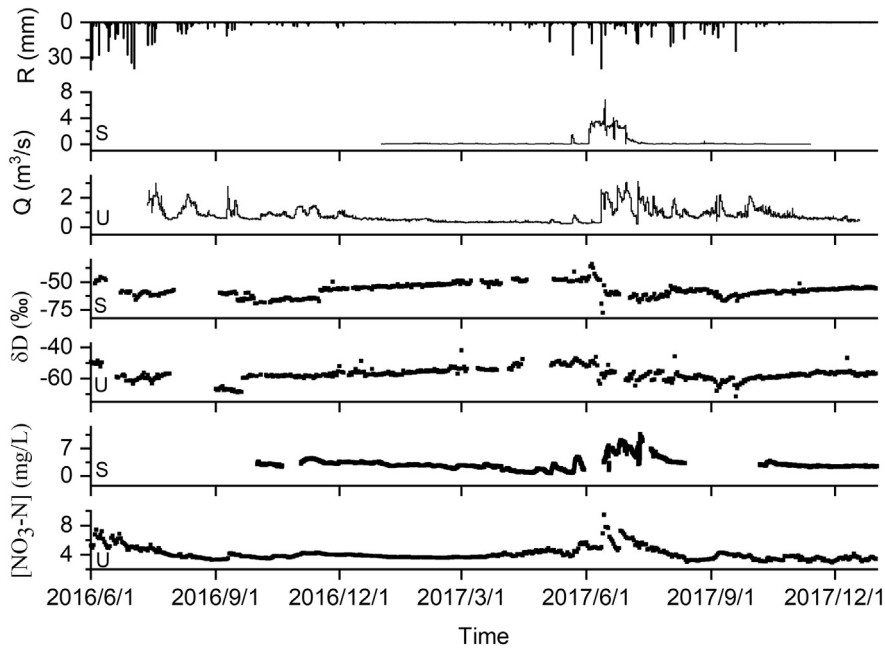
Fig. 3. Time series of rainfall, discharge (Q), δD and [NO₃-N] of surface stream (S) and underground channel (U) at the watershed outlets.

underground channel does. Therefore, among the 47 sinkholes in the catchment (Fig. 1), the 14 in the east are used for flow routing and the remaining 33 sinkholes in the western area are ignored.

2.1.6. Surface stream and underground channel

The Houzhai catchment consists of a surface stream in the north and a main underground channel in the south (Fig. 1). The surface stream, incised an average depth of 2 m below the ground surface, is formed in the relatively thick yellow soil in the north (Fig. 2b). The surface stream is usually dry in drought periods due to the high streambed infiltration into the underlying carbonate aquifer. Only during the flood periods, does the surface stream receive storm water, which flows from two main tributaries to the Qingshan (QS) reservoir and finally to the outlet of the Houzhai River.

The underground channel originates in the eastern mountains where most surface and subsurface flow recharges into the underground drainage network through the eastern sinkholes. The depth of the deep flow zone (underground channel bed or catchment lower boundary) is about 20–40 m below the ground surface (Fig. 3d) (Yu et al., 1990). The upper mountainous region is rich in sinkholes or funnels, which are directly linked with the underground channels, resulting in a responsive hydrograph. When the underground channel reaches the broad and flat plains in the middle and lower catchment, underground flow is more attenuated (Chen et al., 2008).

2.1.7. Catchment sub-division and grid-scale flow routing

For grid routing of the hydrological-nitrogen model, the catchment was divided into a rectangular grid of 100 m × 100 m resolution, totalling 13,000 pixels (104 rows by 125 columns). All the attributes of vegetation, soils, epikarst, and deep zone are assigned in the pixels. The surface stream network is generated automatically following the Horton ordering scheme according to terrain using ARC/INFO. The surface stream width ranges 2–8 m and the depth of the stream bed ranges 1–2.5 m. The underground channel network is manually delineated in terms of field investigation of underground channel information. The underground channel width and depth are approximately 1.5 and 1 m, respectively. ARC/INFO macros are used to subdivide the surface stream and underground channel networks into reaches and to order the cascade branches for the flow routing.

2.2. Hydrochemical observations and analysis

In the Houzhai catchment, two automatic weather stations were established at Chenqi (CQ) and Laoheitan (LHT) (Fig. 1) to record precipitation, air temperature, wind, radiation, air humidity and pressure. The meteorological data and underground channel discharge collection was from 1 March 2016 to 31 December 2017. The discharges of the surface stream and underground channel at the catchment outlet were measured with weirs (Fig. 1). Water levels were automatically recorded by a HOBO U20 water level logger (Onset Corporation, USA) with a time interval of 15 min. The discharge in the surface stream was measured from 1 January 2017 to 31 December 2017.

Rainwater and surface stream and subsurface channel water at catchment outlets were daily sampled between 1 June 2016 and 31 December 2017. All water samples were collected in 5 mL glass vials. The stable isotope ratios of δD and δ¹⁸O were determined using a MAT 253 laser isotope analyser (instrument precision of ±0.5‰ for δD and ±0.1‰ for δ¹⁸O). Water stable isotope ratios are reported in the δ-notation using the Vienna Standard Mean Ocean Water standards. NO₃-N concentrations ([NO₃-N]) at the surface and underground channel outlets were measured using non-optical NISE sensor with a time interval of 15 min from 1 June 2016 to 30 September 2017 (Yue et al., 2019). NH₄-N concentrations were measured several times during June–July 2016.

The discharge, isotopic and NO₃-N concentrations show great variability (Fig. 3). From statistical characteristics of these variables (Table 1), the mean of underground channel discharge is over double that of surface stream discharge while temporal variability of underground channel discharge is much lower than that of surface stream discharge (see CV and Mode in Table 1). The δD ratios of underground channel tend to be less variable than surface stream flow, implying lower influence of young waters. This is particularly apparent for heavy rainfall events (corresponding to the minimum δD value in Table 1) where the young water influence in the underground channel flow is much less than surface stream flow. This suggests that the isotopic responses of underground channel flow and surface stream flow to rainfall are similar in most periods, and only in the heavy rainfall periods, is the surface stream flow newer than underground channel flow.

In terms of mean and maximum values in Table 1, N loading mostly comes from underground channel flow but the peak flow of surface waters can carry the largest N loading. Interestingly, N loading increases

Table 1

Statistical summary of discharge, water stable isotope data, NO_3-N concentration at surface stream and underground channel outlets.

Obs	Surface stream					Underground channel				
	Max	Min	Mean	Mode	CV	Max	Min	Mean	Mode	CV
Discharge (m^3/s)	6.87	0.01	0.32 ± 0.11	0.05	2.69	3.13	0.21	0.79 ± 0.06	1.38	0.63
δD (‰)	−33.7	−77.6	-57.2 ± 0.5	−48.2	0.1	−42	−71.5	-57.4 ± 0.5	−58.8	0.07
NO_3-N (mg/L)	10.71	0.72	3.15 ± 0.25	3.44	0.48	9.78	2.47	4.13 ± 0.33	3.98	0.21

CV: coefficient of variation; ±refers to measured errors.

linearly with discharge for both surface stream and underground channel (Fig. 4), which indicates that variations of the N fluxes are directly proportional to flow. Thus, accurate simulation of hydrographs for hydrological-biogeochemical modelling is vital in this karst landscape. The local meteoric water line (LMWL) is derived from the regression between δ^{18}O and δD values of daily precipitation data sampled between July 2016 and December 2017. The dual-isotope plot shows great evaporative fractionation effects on underground channel flow than surface stream (Fig. 5). The lower slope of underground channel flow illustrates that groundwater in the deep zone mixes more heavy isotopes during infiltration and pecolation.

Monthly wet deposition of NH_4-N and NO_3-N ranged from 0.2–2.6 mg/L for NO_3-N to 0.42–5.8 mg/L for NH_4-N, and monthly dry N deposition was 0.26 kg/ha (Zeng, 2018). Annual fluxes and seasonal distribution of litter fall were estimated drawing on understanding from another basin in Guizhou Province with similar vegetation distributions and geographic conditions (Pi, 2017). Annual fluxes of litter fall range 1.47–3.61 t/ha^{-yr} and the C/N ratios are 18.7–33.1 for forest. The non-point source inputs of N for farm land (paddy and rapeseed) are estimated to be ~270 kg kg/ha^{-yr} (from field surveys by the Karst Ecosystem Research Station of the Institute of Geochemistry in Puding). Leguminous crops are the main N fixation plants, which fix N via symbiotic anaerobic microorganisms (Cheng, 2008). Therefore, for this model,

it is assumed that N-fixation occurs primarily with bean crops, and from field survey in this catchment the fraction of bean crop in each pixel was set to 0.04 in the cultivated land. The rate of annual N fixation by pure
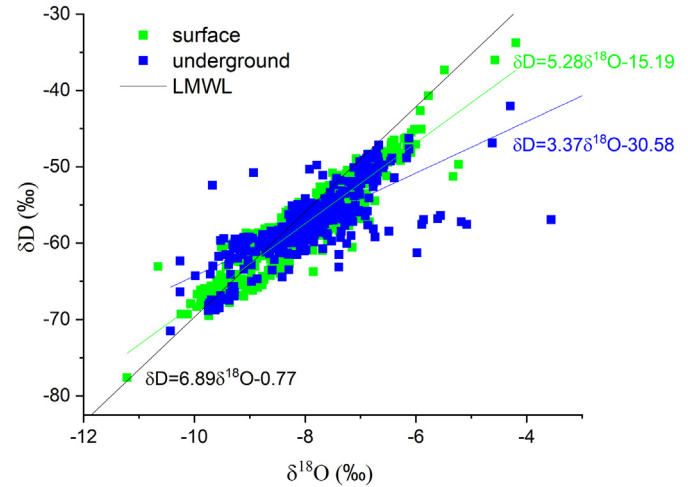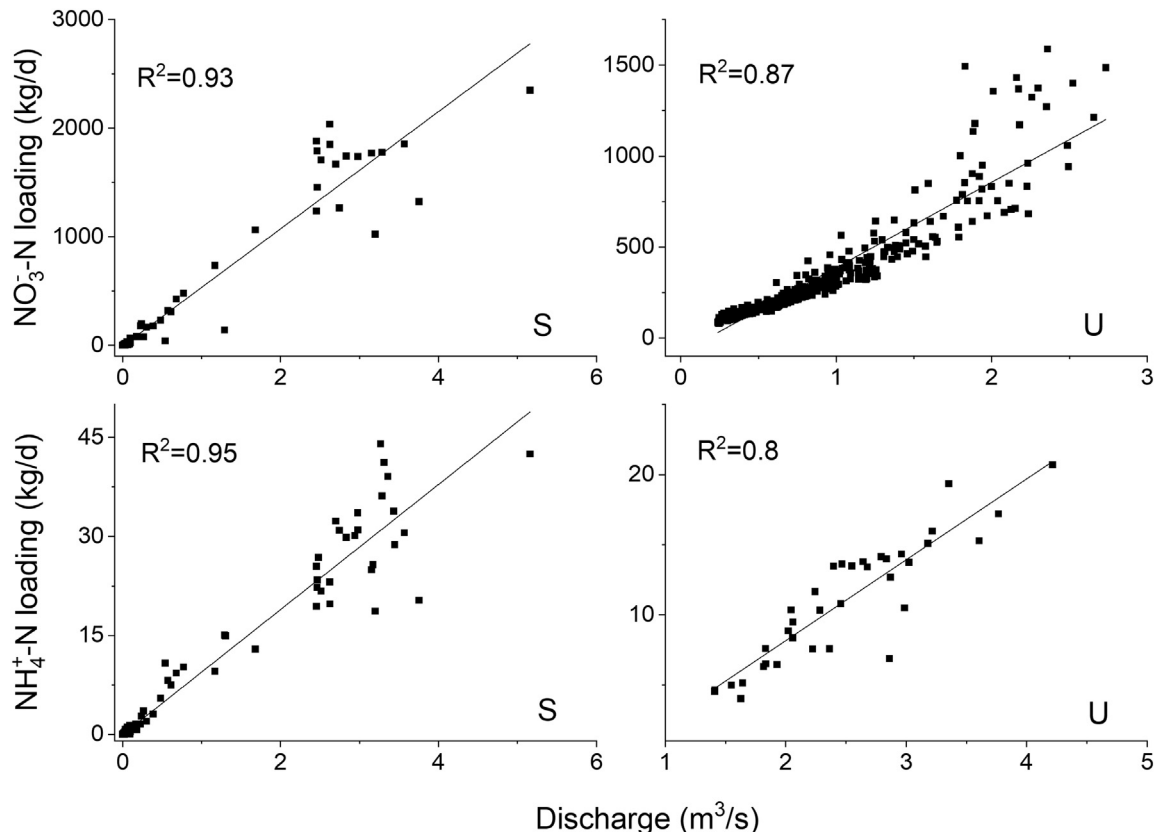

Fig. 5. Dual-isotope plot showing the flow water isotope data at catchment outlet.

Fig. 4. Relationship between daily NO_3-N loading and discharge for surface stream (S) and underground channel (U) at the catchment outlets.

stands of bean was set to 40 kg N/ha^{-yr} (based on Smil, 1999). The potential denitrification fluxes are 6.2×10^{-8} and 1.3×10^{-6} kgN/m^2·h for forest and farm land, respectively (Barton et al., 1999).

3. Model description and execution

The original distributed hydrology-soil-vegetation model (DHSVM) includes a two-layer Penman-Monteith formulation and a two-layer energy balance model for canopy evapotranspiration and ground snow pack, respectively. It contains a multilayer unsaturated soil model, a saturated subsurface flow model, and a grid-based overland flow routing (Wigmosta et al., 1994). The model was subsequently expanded to integrate a biogeochemical module (the DHSVM Solute Export Model, D-SEM) (Thanapakpawin, 2007). To accommodate the special karst geomorphological features, like sinkholes, epikarst and deep aquifers, Zhang et al. (2011) adapted the DHSVM structure for application in Chenqi catchment. The vertical layers of the model are divided to represent vegetation, soils, epikarst, and deep aquifers according to descriptions of karst structure given by Perrin et al. (2003). The flow routing includes sinkhole functions in collecting local surface and subsurface flow in soils and the epikarst zone, and directly connecting these with underground channel outflow (Fig. 6). In this study, the N routings are improved accordingly by conceptualising the above karst geomorphologic functions (Fig. 6), in addition to integrating the mass balance routings and biogeochemical reaction calculations proposed by Thanapakpawin (2007).

3.1. Hydrological simulation

In the three zones of soils (s), epikarst (e) and deep flow zone (d), the flow routings are based on water balance equations for every grid cell in the catchment:

$$\frac{d\theta_s}{dt}d_s = P_0 - P_s(\theta) - E_{to} - E_{tu} - E_s + V_e + (Q_{s,in} - Q_{s,out}) - V_s \quad (1)$$

$$\frac{d\theta_e}{dt}d_e = P_s(\theta) - P_e(\theta) - E_{to} + V_d + (Q_{e,in} - Q_{e,out}) - V_e \quad (2)$$

$$\frac{d\theta_d}{dt}d_d = P_e(\theta) + (Q_{d,in} - Q_{d,out}) - V_d \quad (3)$$

where θ_n is soil moisture and d_n is thickness (n = s, e, d); P_n is infiltrated rainfall (n = 0) or percolated water (n = s, e); E_{to} are E_{tu} evapotranspiration from over story (o) and understory vegetation (u), respectively; E_s is soil evaporation; $Q_{n,in}$ and $Q_{n,out}$ are subsurface flow that passes into and out of the soil, epikarst and deep conduit flow zone, respectively; V_n is return flow.

Vertical infiltration and percolation in the soil (P_s) are estimated based on Darcy's Law assuming a unit hydraulic gradient and using an equivalent hydraulic conductivity as described by Brooks–Corey (1964) for the soils. The "cubic law" is used for estimation of infiltration and percolation of the rock fractures in epikarst (P_e). The spatial distributions of the rock fractures are stochastically generated according to field investigations of fractural characteristics, such as density, length and direction (details in Zhang et al., 2011). The subsurface flow ($Q_{n,in}$, $Q_{n,out}$, n = s, e, d) is calculated cell-by-cell in terms of hydraulic transmissivity ($T = Kd$, where K is hydraulic conductivity, and d is thickness of each layer), hydraulic gradient and the grid width and length (b_{cell} and L_{cell}) at the grid in each flow direction. For the cells within a sinkhole drainage area, surface flow or overland flow (Q_{sur}) and subsurface flow (Q_s and Q_e) directly recharge into the underground channel via the sinkhole ($Q_{sinkhole}$).

In the original DHSVM, flow in surface stream and the underground channel systems is routed using a cascade of linear channel reservoirs
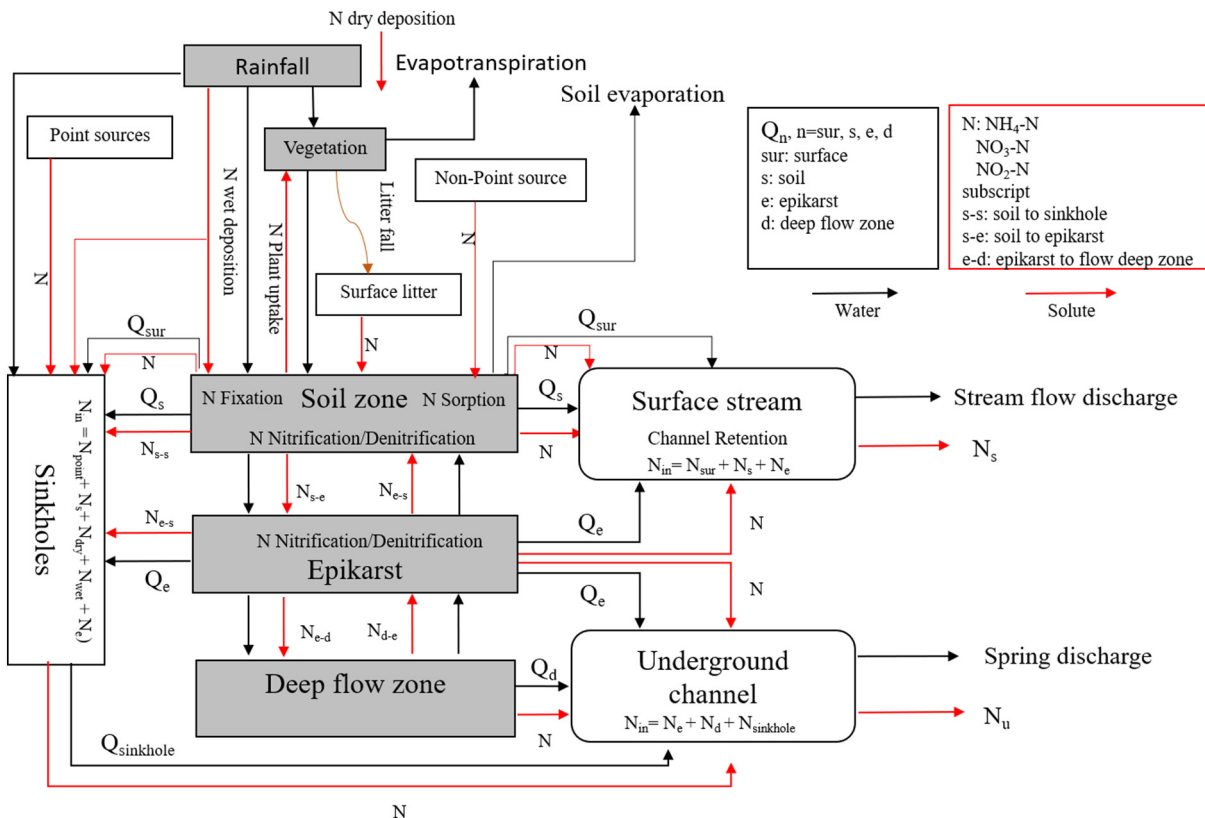

Fig. 6. Schematic representation of the distributed hydrological-N model in karst watershed (D-SEMK). Q_{sur}: overland flow; Q_s: subsurface flow in soil zone; Q_e: subsurface flow in epikarst zone; Q_d: flow in deep flow zone; $Q_{sinkhole}$: flow draining through sinkholes into underground conduit; N: nutrient concentration.

(Wigmosta et al., 1994; Wigmosta and Perkins, 2001). In the new adaptation of DHSVM, for the surface stream flow routing, the lateral flow (Q_{surL}) includes the loss of water as infiltration from the surface stream bed into the underlying aquifer (Q_{inf}), in addition to the gained water of overland flow (Q_{sur}) and subsurface flow in the soil zone (Q_s):

$$Q_{surL} = Q_{sur} + Q_s - Q_{inf} \tag{4}$$

$$Q_{inf} = L_{cell} \cdot b_{cell} \cdot \alpha_{inf} \tag{5}$$

where L_{cell} and b_{cell} are length and width of surface stream segment in one cell, respectively. α_{inf} is constant rate of the surface stream bed. For the underground channel flow routing, the average rate of lateral flow (Q_{gL}) includes the flows from the epikarst zone (Q_e) and the deep zone intercepted by the underground channel (Q_d) when the cells are outside a sinkhole drainage area:

$$Q_{gL} = Q_e + Q_d \tag{6}$$

Otherwise, the lateral flow equals the sinkhole water collected ($Q_{sinkhole}$):

$$Q_{gL} = Q_{sinkhole} \tag{7}$$

3.2. Nitrogen simulation

3.2.1. Mass balance of nitrogen

Consistent with the hydrological module, the karst system is conceptualised as three nitrogen reservoirs in the vertical dimension. The multilayer mass balance model accounts for nitrogen dynamics in the soil, epikarst, and deep flow zones:

$$\frac{dM_s}{dt} = M_{sur-s} - M_{s-e} - M_{s-sur} + (M_{s,in} - M_{s,out}) + \sum_{i=1}^{j_s} M_i \tag{8}$$

$$\frac{dM_e}{dt} = M_{s-e} - M_{e-d} - M_{e-s} + (M_{e,in} - M_{e,out}) + \sum_{i=1}^{j_e} M_i \tag{9}$$

$$\frac{dM_d}{dt} = M_{e-d} - M_{d-e} + (M_{d,in} - M_{d,out}) + \sum_{i=1}^{j_d} M_i \tag{10}$$

where M_n is solute mass ($n = s, e, d$); $M_{n,in}$ and $M_{n,out}$ are mass flux that passes in and out the nth zone, respectively; $\sum_{i=1}^{j_e} M_i (j = s, e, d)$ is biogeochemical mass; subscripts of sur-s, s-sur, s-e, e-s, e-d and d-e represent from surface to soil layer, soil layer to surface, soil layer to epikarst, epikarst to deep flow zone, and deep flow zone to epikarst, respectively.

The solute concentration in each zone can be derived according to the mass (M_n, $n = s, e, d$), the water volume (θ_n, $n = s, e, d$), and the mass fluxes that pass in and out of each zone ($M_{n,in}/M_{n,out}$, $n = s, e, d$). The mass fluxes draining through sinkholes into underground conduits ($M_{sinkhole}$) are calculated from the flows collected by the sinkhole ($M_{sinkhole}$) multiplied by the solute concentration of the collecting water. The model tracks and simulates the solute mass/concentration for each reservoir separately. The solute mass routing in stream channel/underground conduit is based on mass balance:

$$M_{out} = M_{in} + \Delta M_V + \sum_{i=1}^{j_V} M_i \tag{11}$$

$$\sum_{i=1}^{j_V} M_i = M_{sloss} = \varnothing C_{riv\_sur} Q_{riv\_sur} \text{ for surface stream} \tag{12}$$

$$\sum_{i=1}^{j_V} M_i = 0 \qquad\qquad \text{for underground channel} \tag{13}$$

where ΔM_V is mass storage change; $\sum_{i=1}^{j_V} M_i (j = s,e,d)$ is biogeochemical reaction mass; M_{sloss} is retention mass of N in surface stream network; C_{riv_sur} and Q_{riv_sur} are concentration of N and discharge of surface stream at each time step, respectively; $\varnothing$ is coefficient for retention mass of N. The model includes the effects of biogeochemical processes on N concentrations ($\sum_{i=1}^{j_V} M_i (j = s,e,d)$) in the stream channel, but biogeochemical reactivity in the underground water is assumed to be negligible because nitrate is conservative under the oxidizing conditions of many karst aquifer conduits (Perrin et al., 2007; Mahler and Garner, 2009). The N loss in surface stream networks (M_{sloss}) is common (Li et al., 2019), especially in reservoirs within stream networks. Lakebed sediments in reservoir systems can sequester excess nutrients loaded by rivers through sedimentation (David et al., 2006; Saunders and Kalff, 2001). Due to this effect, the reservoirs can be treated as overall sinks for N consequently decreasing downstream nutrient loads (Bosch and Allan, 2008; Powers et al., 2015; Han et al., 2017; Shaughnessy et al., 2019). Therefore, the retention of N in surface stream networks affected by reservoirs was considered using a simple relationship when reservoirs exist in the surface river network (Eq. (12)).

Conservative tracers, such as stable isotopes of hydrogen and oxygen, can be regarded as solutes unaffected by biogeochemical processes. Thus, if the multilayer mass balance model is applied for the solute mass of the tracers, these equations (Eqs. (8) and (10)) can be simplified by neglecting the biogeochemical reactions ($\sum_{i=1}^{j_V} M_i = 0$). Even though stable isotope mass equations add two additional parameters (fractionation coefficients of τ_s and τ_e in soil and epikarst layer, respectively) for considering isotopic fractionation by evaporation (Fig. 6) in the soil and epikarst, the isotopic tracer observations can be used to track hydrological processes and constrain the calibration parameters:

$$M_{s,out} = C_{iso,s} \tau_s (E_{t0} - E_{tu} - E_s) \tag{14}$$

$$M_{e,out} = C_{iso,e} \tau_e E_{t0} \tag{15}$$

where $C_{iso, s}$ and $C_{iso, e}$ are water stable isotope compositions for soil and epikarst, respectively.

3.2.2. Nitrogen sources and biogeochemical processes

Four major N sources are represented in the model: atmospheric deposition, anthropogenic non-point sources, biological N fixation and litter fall. In each time step, the load of atmospheric deposition N is equal to the product of actual deposition concentration and precipitation. Non-point sources, such as fertilizers, are represented on a pixel basis directly. The N-fixation is estimated by (Binkley et al., 1994):

$$N_{fix} = N_f \cdot \varnothing_{T, fix} \tag{16}$$

where, N_f is Nitrogen Fixing Reference Rate; $\varnothing_{T, fix}$ is temperature factor for fixation. Vegetation residue pools from litterfall are divided into a recalcitrant structural pool and a rapidly decomposable metabolic residue pool, each with different decay rates and carbon to nitrogen (C/N) ratios. The N from decomposed litterfall (N_{litter}) is simulated by using a first order rate equation, which is added to the ammonium pool (Inamdar et al., 1999):

$$N_{litter} = A \cdot M / (1 + C/N) \cdot \varnothing_{T,lit} \cdot \varnothing_{\theta,lit} \tag{17}$$

where A is cell area; M is litter mass; $\varnothing_{T, lit}$ is temperature factor for litterfall; $\varnothing_{\theta, lit}$ is moisture factor for litterfall. Soil organic N is not a major source of nitrate in the water samples considering the thin soil profile and rapid water movement in the karst system (Liu, 2009).

Therefore, to reduce the complexity, the organic N processes are not considered in the model focusing primarily on inorganic nitrogen.

Once the N enters soils, it is subject to changes due to biogeochemical processes. After biogeochemical transformation for each time step is completed, the dissolved portion of the pool drains into the surface and underground stream networks. The total amount of nitrification (N_n) and ammonia volatilization (N_{n-v}) is calculated and then partitioned, using a combination of the methods developed by Reddy et al. (1979) and Godwin et al. (1984):

$$N_{n-v} = (1 - \exp(-\varnothing_n - \varnothing_v)) \cdot [NH_4]_L \cdot \frac{1}{24} \tag{18}$$

where

$$\varnothing_n = \varnothing_{T,n} \cdot \varnothing_{\theta,n} \tag{19}$$

$$\varnothing_{T,n} = \begin{cases} 0 \ T \le 4 \\ 2^{\frac{T-O_t}{10}} \ 4 < T < O_t \\ 1 \ T \ge O_t \end{cases} \tag{20}$$

and

$$\varnothing_v = \varnothing_D \cdot \varnothing_{T,n} \tag{21}$$

where $[NH_4]_L$ is mass of NH_4; $\varnothing_{T,n}$ is temperature factor for nitrification, controlled by temperature (T) and the parameter of optimum temperature (O_t); $\varnothing_{\theta,n}$ is moisture factor for nitrification controlled by water content; $\varnothing_D$ is depth factor for volatilization controlled by depth. Then, the nitrification N_n is estimated by:

$$N_n = N_{n-v} \cdot \frac{1 - \exp(-\varnothing_n)}{1 - \exp(-\varnothing_n) + 1 - \exp(-\varnothing_v)} \tag{22}$$

The calculation of denitrification (N_d) is modified from Hénault and Germon (2000):

$$N_d = D_p \cdot \varnothing_{T,d} \cdot \varnothing_{No3} \cdot \varnothing_{\theta,d} \tag{23}$$

and

$$\varnothing_{\theta,d} = \begin{cases} 0 \ f_{sat} < D_{st} \\ \left(\frac{f_{sat} - 0.62}{0.38}\right)^{1.74} \ f_{sat} \ge D_{st} \end{cases} \tag{24}$$

$$\varnothing_{No3} = \frac{[NO_3]}{(R_{hs} + [NO_3])} \tag{25}$$

where D_p is potential denitrification flux; $\varnothing_{T,d}$ is temperature factor for denitrification controlled by temperature; $\varnothing_{\theta,d}$ is moisture factor for denitrification controlled by parameter of denitrification saturation threshold (D_{st}); f_{sat} is soil moisture saturation extent; $\varnothing_{No3}$ is nutrient factor controlled by nitrate reduction half saturation fraction (R_{hs}).

Michealis-Menton saturation kinetics are assumed to be the mechanics of plant NH4-N uptake ($NH_{4, uptake}$) (Yao et al., 2011; Bicknell et al., 1993), and its calculation includes the parameters of Half-rate Ammonium Uptake Constant (Au) and Maximum Ammonium Uptake Constant (Aum):

$$NH_{4,uptake} = \frac{Aum \cdot [NH_4]_L}{Au + [NH_4]_L} A \tag{26}$$

For NO3-N uptake ($NO_{3, uptake}$), the model used is a modified yield-based approach, with the parameters of Maximum Nitrogen Uptake

Delay (Num) and Maximum Nitrogen Accumulation (Nam):

$$NO_{3,uptake} = Nam \cdot \frac{\exp\left(-\frac{((t)_c - t_{sta} - Num)^2}{2 \cdot \left(\frac{t_{long}}{3}\right)^2}\right)}{\left(\frac{t_{long}}{3}\right) \cdot \sqrt{2\pi}} \tag{27}$$

where t_c is current day; t_{sta} is growing season start day; t_{long} is growing season length.

A simplified scheme to represent sorption as a function of NO_3-N ($NO_{3, sorption}$) and NH_4-N ($NH_{4, sorption}$) mass was used in the model:

$$NO_{3,sorption} = M_{NO_3} \cdot N_a \tag{28}$$

$$NH_{4,sorption} = M_{NH_4} \cdot A_a \tag{29}$$

where M_{NO3} and M_{NH4} are NO_3 and NH_4 mass, respectively; N_a is Nitrate Sorption Coefficient; A_a is Ammonium Adsorption Coefficient.

These biogeochemical reactions are assumed to occur in the soil layer in non-karst areas (see Thanapakpawin (2007) for detail). In our modified model, the nitrification and denitrification of N occur in both the soil and epikarst zones.

3.3. Modelling procedures

All simulations were performed on hourly time steps, at a 100×100 m^2 resolution. The hourly discharge, daily water stable isotope composition and NO$_3$-N concentration were used for the model calibration. Automatic calibration of the coupled hydrological-N model at such a high spatiotemporal resolution is very time consuming. Therefore, the step-by-step method was employed for parameter estimation (Ferrant et al., 2011). The parameters of hydrological module are optimized first, and then parameters for biogeochemical reactions were manually calibrated using the optimized hydrological parameters.

The parameters of the hydrological module can be divided into sensitive and insensitive parameters (Yao, 2006; Kelleher et al., 2015). The insensitive parameters were determined as follows: (1) the vegetation-related parameters were determined by the field investigations, such as the height of 2.1 and 1 m for forest and crops, respectively; other parameters (e.g. LAI, albedo and root depth) were based on the Land Data Assimilation System (LDAS); (2) the soil-related parameters, such as bulk density, porosity and wilting point, were measured using field experiments and laboratory analysis (Cheng et al., 2011); and (3) the other insensitive parameters, such as pore size distribution, aerodynamic attenuation and moisture threshold, were drawn from literature (e.g., Thyer et al., 2004; Kelleher et al., 2015). The sensitive parameters, e.g. hydraulic conductivities (K_h and K_v), field capacity (θ_f) in the soils, epikarst and deep zones, and canopy fraction (C_f) in Table 2, were calibrated against observations of discharge within the initial ranges of the sensitive parameter in Table 2. In order to reduce equifinality effects, these sensitive parameters together with two additional parameters (fractionation constants of τ_s and τ_e in Table 2) are further calibrated against observations of isotopic ratios.

The modified Kling–Gupta efficiency (KGE) criterion (Kling et al., 2012) was used as the objective function for flow and isotope calibrations. The criterion balances how well the model captures the dynamics (correlation coefficient), bias (bias ratio) and variability (variability ratio) of the actual response (Schaefli and Gupta, 2007). The objective functions of KGE for the surface stream and underground channel were combined to formulate a single measure of goodness of fit. Targeted on the flow discharge, the objective function is KGE$_Q$ = (KGE$_{Q-sur}$ + KGE$_{Q-und}$) / 2 (where KGE$_{Q-sur}$ and KGE$_{Q-und}$ are the objective functions for surface stream and underground channel discharges, respectively). Targeted on the isotopic concentration, the objective function is KGE$_i$ = (KGE$_{i-sur}$ + KGE$_{i-und}$) / 2 (where KGE$_{i-sur}$ and KGE$_{Q-}$

Table 2
Ranges of hydrological parameters and fractionation coefficients for random sampling.

	Parameter	Range		Parameter	Range
Yellow soil	K_h (m/s)	1×10^{-6}–1×10^{-4}[a] 5×10^{-6}–5×10^{-5} (2×10^{-5})	Epikarst	K_h (m/s)	1×10^{-5}–1×10^{-3}[a] 2×10^{-5}–2×10^{-4} (5×10^{-5})
	K_v (m/s)	1×10^{-6}–1×10^{-4}[a] 2×10^{-6}–2×10^{-5} (1×10^{-5})		K_v (m/s)	1×10^{-5}–1×10^{-3}[a] 7×10^{-5}–6×10^{-4} (4×10^{-4})
	θ_f	0.1–0.5[a] 0.2–0.37 (0.35)		θ_f	0.01–0.15[a] 0.01–0.1 (0.02)
Paddy soil	K_h (m/s)	1×10^{-7}–5×10^{-5}[a] 3×10^{-6}–2×10^{-5} (1×10^{-5})	Deep flow zone	K_h (m/s)	1×10^{-7}–1×10^{-5}[a] 3×10^{-6}–8×10^{-6} (4×10^{-6})
	K_v (m/s)	1×10^{-7}–5×10^{-5}[a] 1×10^{-6}–1×10^{-5} (9×10^{-6})		K_v (m/s)	1×10^{-7}–1×10^{-5}[a] 2×10^{-6}–9×10^{-6} (3×10^{-6})
	θ_f	0.1–0.5[a] 0.25–0.42 (0.38)		θ_f	0.01–0.15[a] 0.01–0.05 (0.01)
Lime-stone soil	K_h (m/s)	1×10^{-6}–5×10^{-4}[a] 1×10^{-5}–1×10^{-4} (6×10^{-5})	Forest		0.5–1[a] 0.6–0.9 (0.85)
	K_v (m/s)	1×10^{-6}–5×10^{-4}[a] 1×10^{-5}–8×10^{-5} (4×10^{-5})	Farm land	C_f	
	θ_f	0.1–0.5[a] 0.15–0.31 (0.18)			0.5–1[a] 0.5–0.9 (0.6)
Fractionation coefficient	τ_s	1–5[a] 1–3 (2.8)		τ_e	1–5[a] 1–2 (1.6)

The values in brackets represent the mean of the best 114 parameter sets after calibration.
  [a] Represents the initial range for the first sampling.

und are the objective functions for isotopic concentrations for surface stream and underground channel, respectively).

A Monte Carlo analysis was used to explore the parameter space during calibration and provides insight to the resulting uncertainty. In order to derive a constrained parameter set, two iterations were carried out in the calibration. First, a total of 2000 different parameter combinations within the initial ranges was randomly generated as the possible parameter combinations (Soulsby et al., 2015; Xie et al., 2018). After the first calibration using KGE_Q and $KGE_i > 0.3$ was used as a threshold for model rejection, and the range of each parameter was narrowed. Then, another 2000 different parameter combinations within the narrowed ranges were used as for the second calibration, and the parameter space was reduced by iteratively applying two criteria: 1) the discharge criterion discarded all parameter sets that obtain a $KGE_Q < 0.75$, and 2) the water stable isotope criterion discarded all parameter sets that obtain a $KGE_i < 0.5$. The retained parameter sets were further used for simulation of possible flow discharges and the tracer compositions, and their uncertainty bands. In addition to KGE, root mean squared error (RMSE) and absolute of average relatively error (aARE) were calculated for evaluation of the model performance.

After determining the best hydrological parameter set (it consists of the mean values of each parameter derived from the retained parameter sets after calibration), the N module parameters related to biogeochemical reactions (Table 3) were manually calibrated using the observed NO_3-N concentrations at the catchment outlets. The values of the biogeochemical parameters used in Thanapakpawin (2007) were taken as the initial values for model running. Then these parameters for biogeochemical reactions were calibrated against the best matching NO_3-N concentrations measured at the outlets. Comparisons of the simulated and measured NH_4-N concentrations at the catchment outlets were used as a "soft" validation of the simulations. This strategy of the

model calibration was also used in other studies for the complex simulation of biogeochemical reactions (Zhang et al., 2016, 2017a).

The modelling period started on 1 March 2016, but calibration was initiated using available discharge data from 13 July 2016 and isotopes from 1 June 2016. The preceding four months were therefore used as a spin-up period (the mean of precipitation isotope signatures over the sampling period was used for this) to fill storages, and initialise storage tracer and N concentrations.

4. Results

4.1. Model performance

The modelling results show that the discharge dynamics in surface stream and underground channel were mostly bracketed by the simulation ranges at the outlet though some discharges were not completely captured (Fig. 7). The objective function values of the combined KGE_Q for flow discharge at the outlets were all >0.75 for the 114 retained parameter sets, with a maximal value of 0.81 and the mean of 0.77 over the study period. The maximal, mean and minimal objective function values were 0.8, 0.77 and 0.7, respectively, for surface stream discharge ($KGE_{Q\text{-sur}}$), and 0.82, 0.78 and 0.72, respectively, for underground channel discharge ($KGE_{Q\text{-und}}$). The mean of RMSE and aARE is 0.31 m³/s (0.23–0.39 m³/s) and 10% (6%–16%), respectively, for surface stream discharge, which is larger than 0.28 m³/s (0.21–0.35 m³/s) and 7% (4%–13%) for underground channel. The simulated results capture the surface stream flow during the heavy rainfall periods (Fig. 7).

The simulated water stable isotope ratios show that the model generally reproduces the overall δD signal of surface stream and underground channel water during study period (Fig. 8). The combined KGE_i for water stable isotope composition at the stream and underground channel outlets were all >0.5, with a mean of 0.62 and maximal value of 0.67. The mean of RMSE and aARE is 8.9‰ (5.7–10.9‰) and 12% (8%–19%), respectively, for surface stream discharge, which is larger than 5.6‰ (3.5–7.6‰) and 11% (6%–16%) for underground channel. As is common in coupled flow-tracer models, the performance in the simulation of water stable isotopes was less satisfactory and more uncertain than for discharge (Table 4). There were some enriched "outliers" in underground channel water with high isotope values out of the uncertainty range (the maximum of δD less than −50‰). The most likely explanation for this is flooded paddy fields, which are extensively distributed in the depression during the growing season; this allows

Table 3
Calibrated parameters for biogeochemical reaction of N.

Parameters	Forest	Farm land	Soil & epikarst		Surface channel	
N_f (kg/ha-yr)	–	40	D_{st}	0.6	$\varnothing$	0.35
Num (day)	180	160	R_{hs}	0.5		
Nam (mg/m²)	3000	800	O_t	5		
Au (kg)	3.6×10^{-3}	3.7×10^{-3}	L-s	0	L-s	0.01
Aum (kg)	3.9×10^{-4}	4.02×10^{-4}	N_a P-s	0.01	A_a P-s	0.03
C/N	25	40	Y-s	0.01	Y-s	0.03

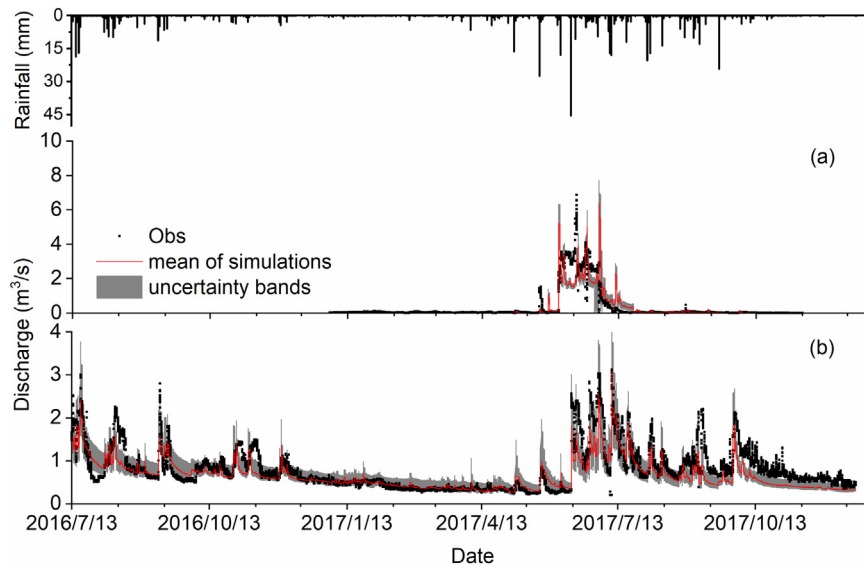L-s: limestone soil, P-s: paddy soil, Y-s: yellow soil.

Fig. 7. The simulated and observed discharges at surface stream outlet (a) and underground channel outlet (b) over the study period. Note: Observations are shown with black symbols while the red line displays mean of the simulations for the 114 retained parameter sets after calibration.
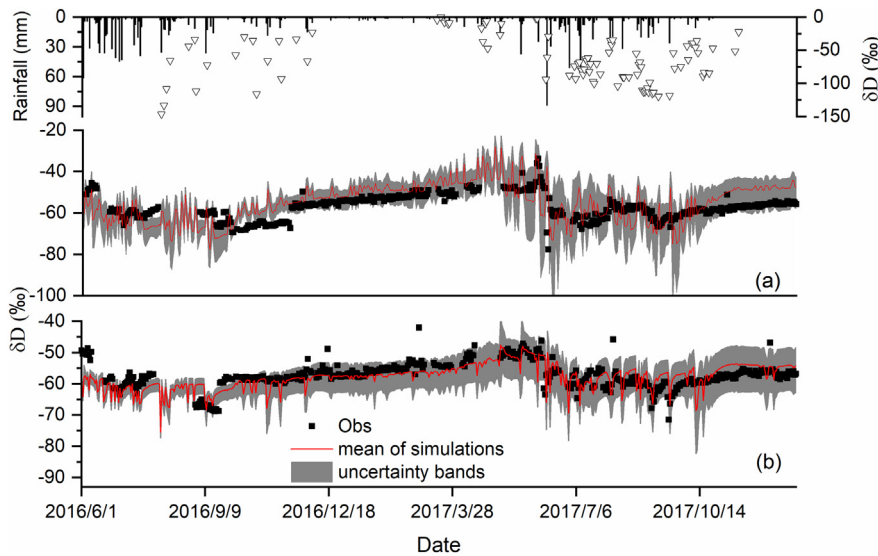

Fig. 8. The simulated and observed deuterium ratio in the surface stream (a) and underground channel outlets (b) over the study period. Note: Measurements are shown with black symbols while the red line displays mean of the simulations for the remaining parameter sets.

Table 4
Performance metrics of discharge, δD and [NO₃-N] for surface stream and underground channel at catchment outlet.

Performance metrics		Surface stream			Underground channel		
		Discharge	δD	[NO₃-N]	Discharge	δD	[NO₃-N]
RMSE	Max	0.39	10.9	–	0.35	7.6	–
	Min	0.23	5.7	–	0.21	3.5	–
	Mean	0.31	8.9	1.06	0.28	5.6	0.37
aARE	Max	0.16	0.19	–	0.13	0.16	–
	Min	0.06	0.08	–	0.04	0.06	–
	Mean	0.10	0.12	0.14	0.07	0.11	0.12
KGE	Max	0.80	0.65	–	0.82	0.7	–
	Min	0.70	0.44	–	0.72	0.51	–
	Mean	0.77	0.53	0.45	0.78	0.61	0.5

RMSE represents root mean squared error (m³/s, ‰ and mg/L for discharge, deuterium ratio and [NO₃-N], respectively), aARE represents the absolute of average relatively error, and KGE represents efficiency.

evaporative fractionation effects which are transferred to the channel network in larger events Zhang et al. (2019).

Although the performance of the coupled flow-tracer model for isotope simulation was less accurate than for discharge simulation, targeting both the flow discharge and isotopic concentration (e.g. meeting KGE_Q ≥ 0.75 and KGE_i ≥ 0.5) can effectively narrow the parameter ranges and thus reduce equifinality effect of these additional parameters on the simulated results (Fig. 9).

The calibrated parameters for modelled biogeochemical reactions for N are listed in Table 3. The modelled results with this parameter set show that the simulated daily NO₃-N concentrations can generally capture the observations at the outlets of the surface stream and underground channel (Fig. 10). The simulated uncertainty of NO₃-N is larger than that of discharge and isotopic profile as the model structure becomes more complex and the number of calibrated parameters increases. The KGE_N-sur and KGE_N-und for daily NO₃-N concentrations were 0.45 and 0.5 at surface stream and underground outlets,
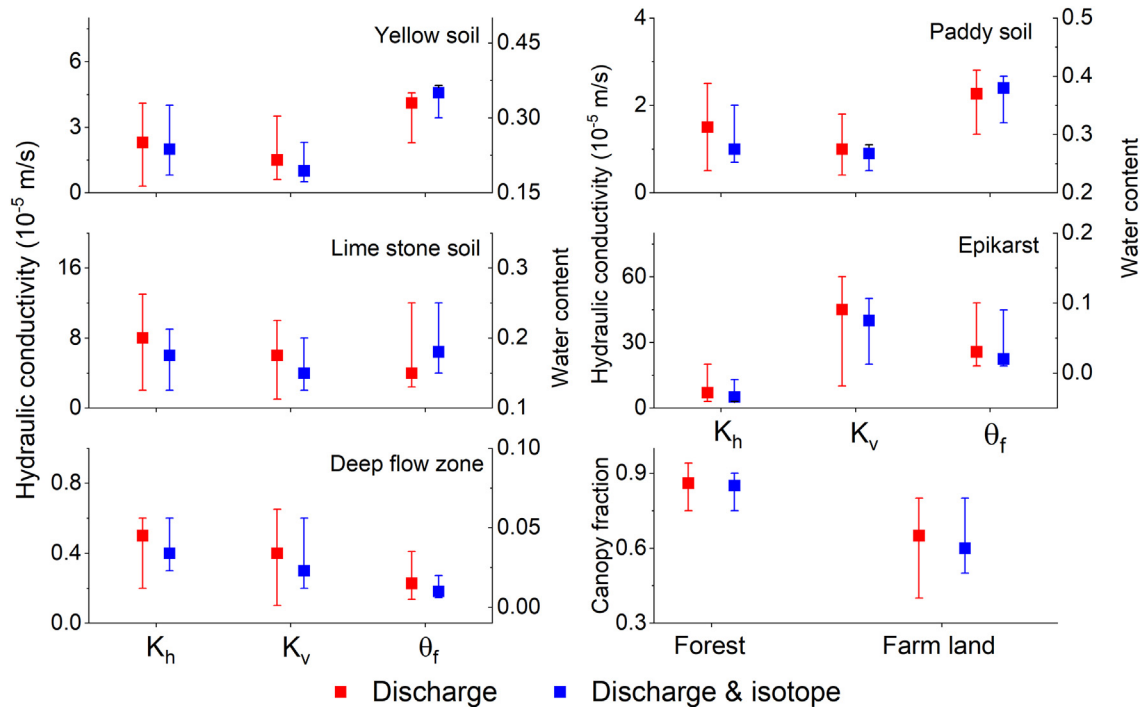
Fig. 9. Comparison of the calibrated parameters for hydrological module that the discharge target meets $KGE_Q \geq 0.75$ and the combination target of discharge and isotopic concentration meets $KGE_Q \geq 0.75$ and $KGE_i \geq 0.5$.

respectively. The mean of RMSE and aARE is 1.06 mg/L and 14% respectively for surface stream, both >0.37 mg/L and 12%, respectively for underground channel. The larger deviation of the simulated N in surface river could result from complex flow regulation and biogeological processes in the reservoir (Wang et al., 2020).

The measured NH_4-N concentrations at the outlets were further used to test the model performance. Since the NH_4-N concentrations of water in the study area were very low ($\sim 10^{-2}$ mg/L) (smaller than the calculation errors of the mixing and biogeochemical processes of NH_4-N), the simulated results cannot capture variability but the magnitude of the simulated and measured concentrations is of the same order for both the surface stream and underground channel outlets (Fig. 11). The mean measured and simulated NH_4-N concentrations are 0.05 and 0.06 mg/L, and the total measured and simulated loadings of NH_4-N are 224 and 262 kg, respectively, for surface river during the observation period (a total of 30 days). For underground channel, both the mean measured and simulated NH_4-N concentrations are 0.05 mg/L, and the total measured and simulated loadings of NH_4-N are 341 and 343 kg, respectively, over the observation period (a total of 38 days).

4.2. Vertical and spatial distributions of the simulated NO_3-N storages

Fig. 12 shows the spatial distribution of simulated NO_3-N loadings (concentrations of NO_3-N multiplied by the flux in each layer) in the three layers of the critical zone. Spatial variations of the NO_3-N loadings in soils are most marked because of spatial difference of soil thickness, hydraulic conductivity and land cover. NO_3-N loadings in the relatively thick soils in the western plain are mostly larger than those in the thin soils in the eastern mountains (Fig. 12a). In spite of thin soils over the whole catchment, the soil layer was the largest NO_3-N store in the catchment (Fig. 12). The average values of NO_3-N in the soil, epikarst and deep flow layers are 58.4, 18.6 and 15.3 kg/ha, respectively. In each of the layers, the NO_3-N loadings in the farm land are much larger than those in the forest areas (Fig. 12d). For example, the annual NO_3-N loading is 452 and 40 t for the soil layers in the farm land and forest respectively. The greater NO_3-N loading in the farm land is mainly

attributed to the high fertilization rates in this region (e.g. the NO_3-Ns for paddy soil and yellow soil were 67 and 53 kg/ha, respectively).

4.3. Simulated exchanges of N fluxes in the critical zone and catchment N balance

Fig. 13 shows daily and cumulative net input and the simulated loss of N from 13 July 2016 to 31 October 2017 in the catchment. Atmospheric deposition, litter fall and fixation show less seasonal variability. The much greater N input (the short lines in Fig. 13) indicates fertilizer input in farm land, shown by a marked increase of the cumulative input occurred in the fertilizer period in May–early June. The greatest input results in a prolonged increase of N loading for the high discharge in the wet season from May to September in this catchment.

The simulated nitrification and denitrification rates of N over the study period clearly showed a seasonal variability with temperature and wetness in a year (Fig. 14). The daily rates of nitrification and denitrification are much higher in wet season (0.34 and 0.21 kg N/ha for nitrification and denitrification, respectively) than in dry season (0.01 and 0.06 kg N/ha, respectively). The peaks of nitrification and denitrification occur in the fertilizer periods. The highest peaks of nitrification and denitrification rates (2.7 and 0.53 kg N/ha, respectively) correspond to the heaviest fertilization in May–early June.

The simulated annual N fluxes (including NO_3-N and NH_4-N) between the layers in the critical zones are shown in Fig. 15. For the total input of N (1417 t) from atmospheric deposition (149 t), fertilizer (1220 t), litter fall (42 t) and fixation (6 t) in the catchment during the study year, fertilizer accounts for 86%. These inputs are mainly consumed by terrestrial plant uptake (~636 t), accounting for about 45% of the total input of N. The remaining losses are from ammonia volatilization (~118 t), denitrification (~396 t), and surface channel retention (~31 t), and exports from the catchment via the surface stream (58 t) and underground channel (135 t).

From the total input of N (1417 t) to the soil layer, 254 t of N leaches into the underlying epikarst zone, and 97 t of N is transported to the surface stream and subsurface channel, 636 t of N is absorbed by plant, 278 t is denitrified, and 83 t is volatilized. Of the 254 t of N which drains
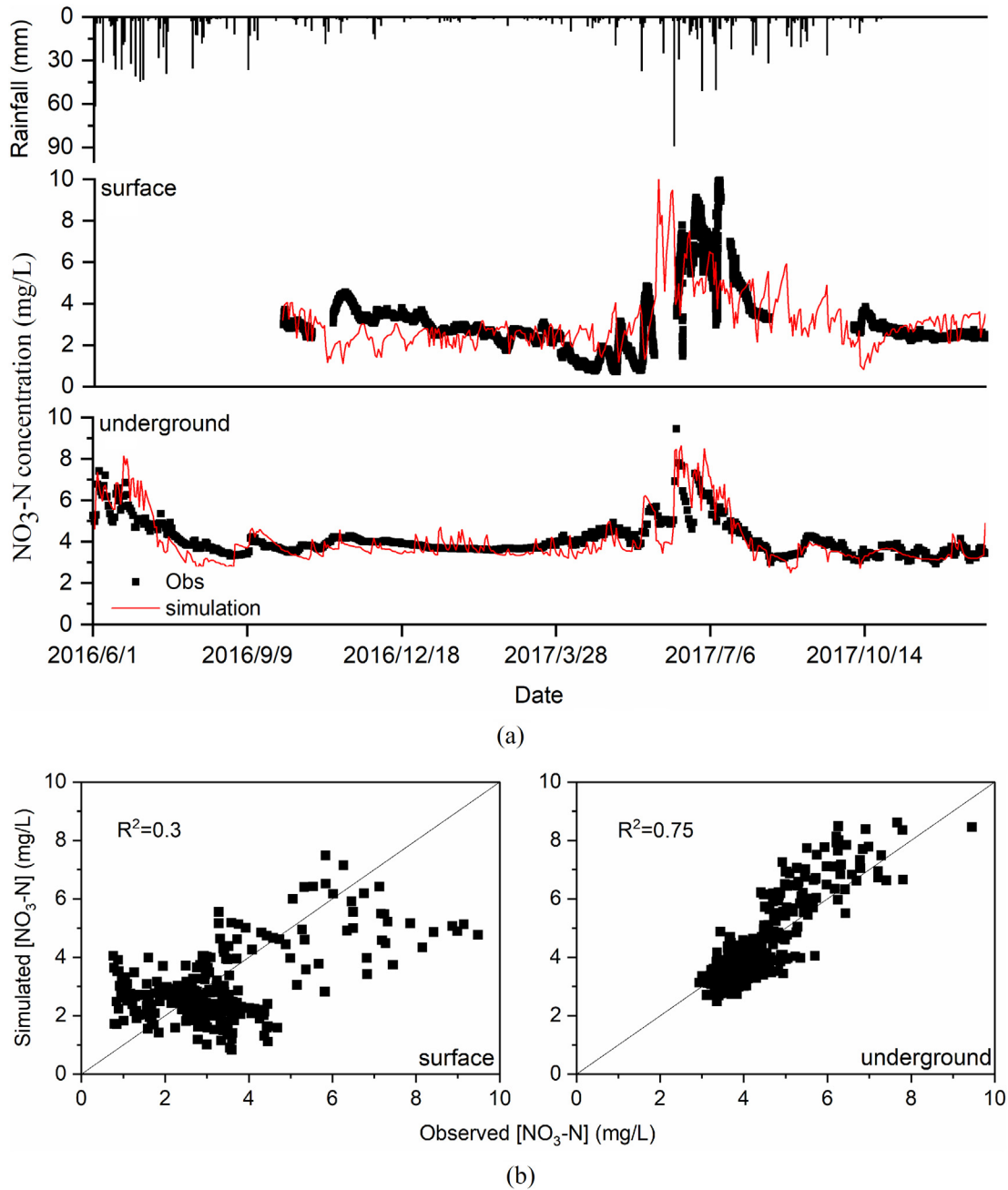
Fig. 10. The simulated and observed NO$_3$-N concentrations (a) and the correlation between them (b) for surface stream and underground channel over the study period.

into the epikarst zone, nearly half of it (108 t) is transported to the subsurface channel, 118 t of N is denitrified, 35 t is volatilized, and only 15 t drains into the deeper aquifer. The large flux of N from the epikarst to the subsurface channel results in greater annual export of N from underground channel (135 t), compared to the surface stream (58 t).

5. Discussion

5.1. Uncertainty of the simulation with increased model complexity

The hydrological-biogeochemical model in this study was developed by considering flow and N fluxes in the karst critical zone characterized by special geomorphologic conditions, such as fractured zone (epikarst) and sinkholes that interconnect with surface and subsurface streams. Even though there are still uncertainties for the modelling results, particularly for the N simulations, the model can simulate the concurrent dynamics of hydrological, isotopic and N processes in the catchment. It was found that N loading is linearly proportional to discharge for both surface stream and underground channel at the catchment outlet (Fig. 4), and thus capturing hydrological dynamics for the model, aided with detailed hydro-chemical observations, are essential for controlling the N-loading variations in this karst catchment. In order to capture hydrological dynamics and reduce uncertainties arising from increasing complexity of the model structure and associated parameterisation (e.g. increase of the vertical zones and the related parameters), we constrained hydrological module parameter ranges in the model calibration by using a combination of observations of flow discharges and isotopic concentrations. We found that although the isotope-aided model introduced two additional parameters, the detailed observations of isotopic concentrations can narrow the parameter ranges and thus reduce equifinality effect of parameters on the simulated results (Fig. 7).
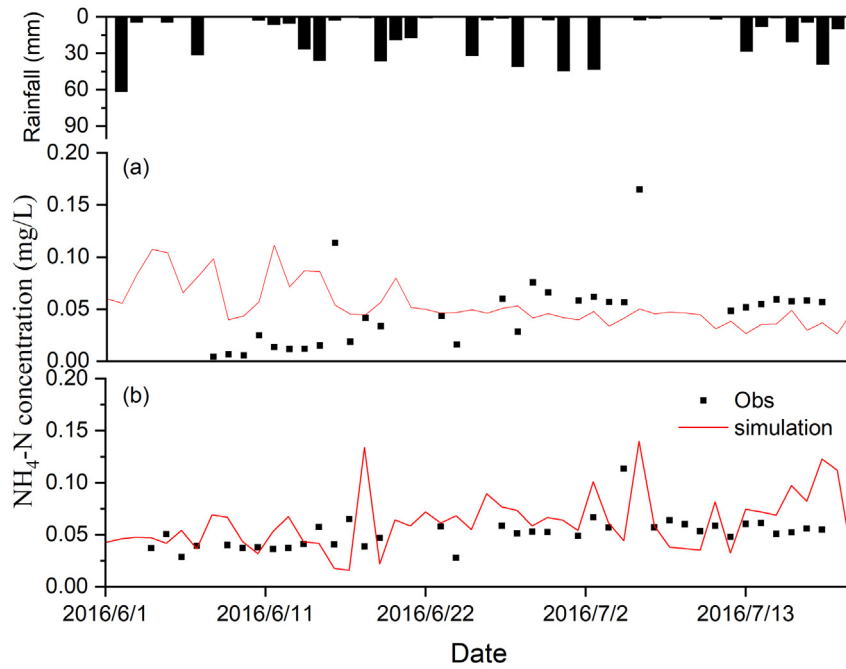
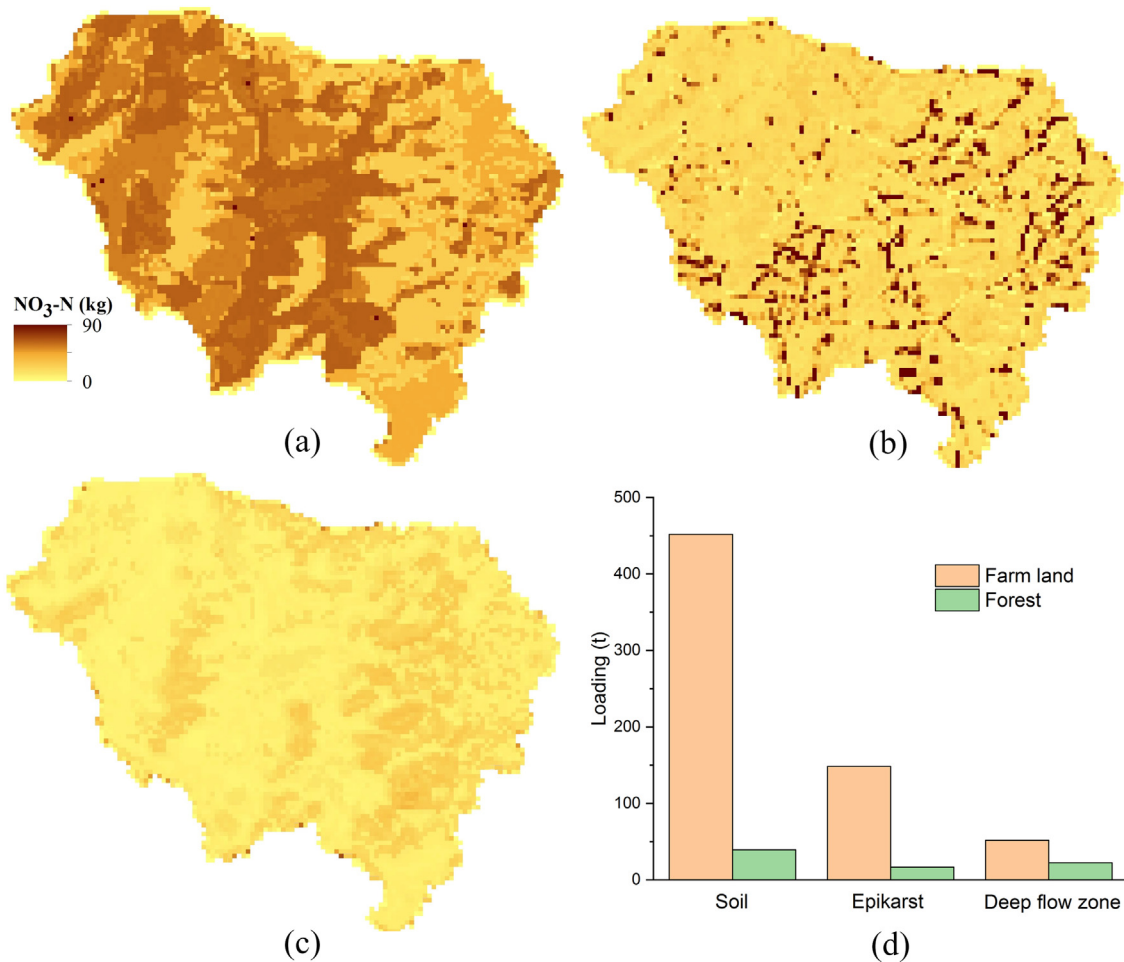**Fig. 11.** The simulated and measured NH₄-N concentrations at surface stream (a) and underground channel (b) over the study period.

Fig. 12. The simulated spatial distribution of mean NO₃-N loadings in each layer during the study period in Houzhai catchment. (a) Soil layer, (b) epikarst, (c) deep flow zone, and (d) the annual NO₃-N loading in each store with different land cover.
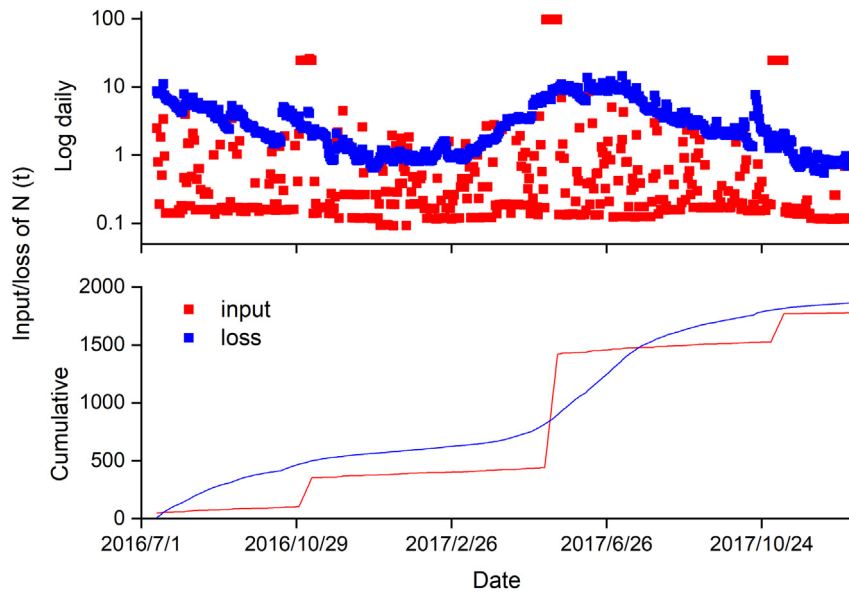
Fig. 13. Daily (a) and cumulative (b) inputs and losses of N from Houzhai catchment.
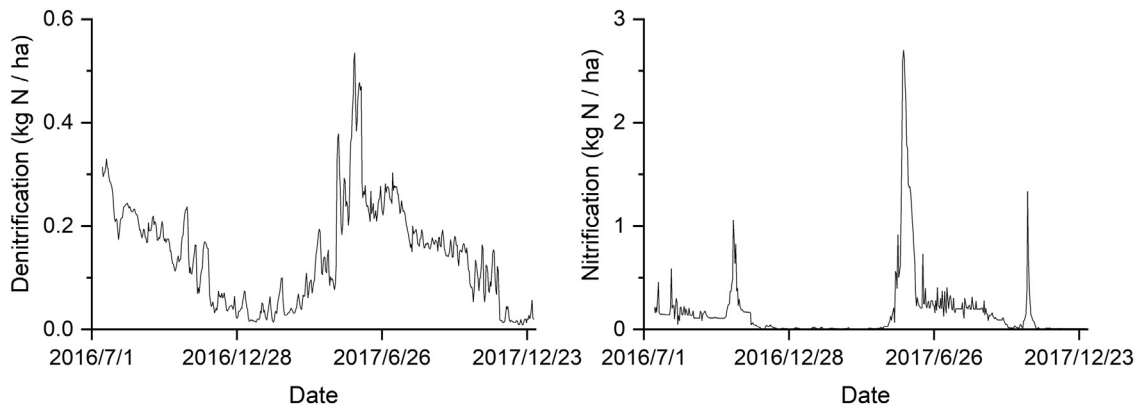
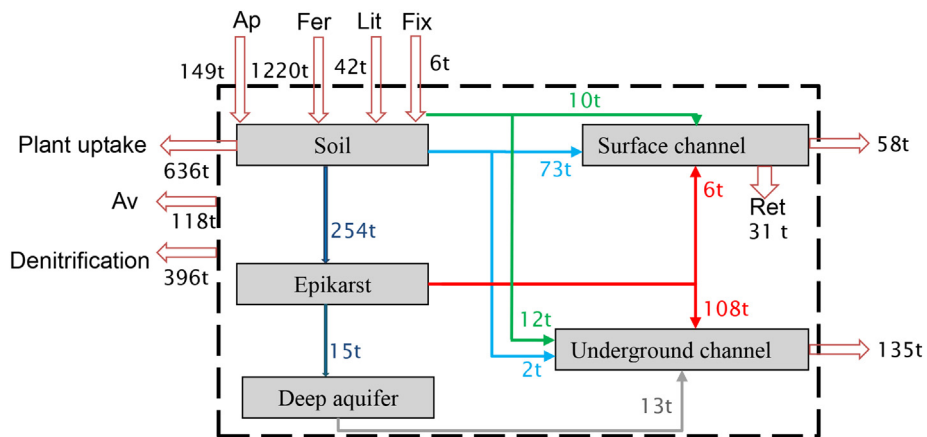Fig. 14. Simulated daily nitrification and denitrification of N.

Fig. 15. Simulated annual N fluxes and loadings in each modelled reservoir. The karst system of the catchment is in the dotted wire frame. Red hollow arrows represent the annual N flux into and out the system. The coloured solid arrows represent the annual N flux within the karst system. Note: **Ap**: Atmospheric deposition; **Fer**: Fertilizer; **Lit**: Litter Fall; **Fix**: Fixation; **Av**: Ammonia volatilization; and **Ret**: Surface channel retention.

The relatively larger uncertainties of N simulations arise from increasing complexity of the model structure, and from observations of N and calibration procedures. For example, the N inputs were estimated from field surveys at some specific sites (e.g., the fertilizer and the fraction of bean production), from measurements in other areas (e.g., litter fall), and from other research (e.g., the referenced rate of annual N fixation from Smil (1999)). Even though high temporal resolution of N concentrations has been monitored at the catchment outlets, more detailed observations and field surveys of these inputs are required to reduce uncertainty in the complex hydrological and biogeochemical processes.

The parameter calibration in this study employs a step-wise procedure of targeting simulation accuracies of outlet discharges and water stable isotope ratios for the hydrological module, and then the NO_3-N concentrations for the biogeochemical module. The procedure is computationally efficient for complex model calibration in terms of the Monte Carlo framework, but it weakens interactions between hydrological and biogeochemical dynamics. In future research, simultaneous calibration of the hydrological-biogeological model parameters by combining use of hydrological observations, isotopic analysis (including N isotope analysis) and N concentrations may help further constrain the parameter ranges and reduce uncertainty of N simulations.

5.2. N sources and pathways in karst landscapes

Assessing N sources and transfer pathways is an evidence base for promoting efficient use of N and preventing N loss, thereby improving N management at the catchment scale (Pionke et al., 1996; Heathwaite et al., 2005; Jarvie et al., 2008, 2017; Kovacs et al., 2012). Our distributed model provides quantitative information on N sources and loads (Fig. 15), which are essential for catchment managers who need to make evidence-based decisions on N pollution controls. In this catchment, about 61% of N export occurred during the wet season, because of the large stream flow during that time. This is driven by the high water flux transporting large amounts of N from the soil reservoir into the epikarst and deep flow zone, and then into the surface and underground channels. Therefore, the quick response of water flow to rainfall usually leads to the concentrated export of N in karst catchments. Many studies have indicated that delivery times for soil water, shallow groundwater and deep groundwater to river systems range from years to decades in non-karst areas (Sanford and Pope, 2013). The considerable contribution of N loading to streams from groundwater (e.g. 67% groundwater contributions to river N loading in Yongan catchment in southeast China) leads to a marked lag effect of N flux (Hu et al., 2018). However, the epikarst reservoir in the Houzhai catchment contributes the most N to the surface stream and underground channel (~45%, in Fig. 15) through fractures/conduits in the karst, which implies the potential for a low hydrologic lag effect of N flux due to the high hydraulic conductivity of epikarst (5×10^{-5}–4×10^{-4} m/s in Table 2).

The limited soils in karst areas are extremely important for sustaining crop and plant growth. The simulated spatial distributions of NO_3-N indicated that the main reservoirs and sources of N are located in the cultivated land of low lying plain and valley areas with relatively thick soil cover in southwest China. Meanwhile, the frequent, heavy fertilization accentuates N accumulation in the farm land, and this makes these areas the main sources of N loss during rainstorm periods. In addition, the soil properties and underlying rocks also have marked influences on N loading and export. Under the same effect of fertilization, the N loading of the soil reservoir in yellow soils in the dolostone was markedly lower than that with paddy soil in the limestone, because of the higher infiltration and percolation rates.

Sinkholes are another important transport and export pathway. Sinkholes sometimes function as storm drains because they directly link to the underlying aquifer systems (Tihansky, 1999). In the upstream area with more sinkholes, over 90% of the N export was in the wet season (Yue et al., 2019). However, the importance of N flux through sinkholes in karst areas is a relatively under-researched topic in soil and water science.

5.3. Implications for fertilization management in karst areas

Agricultural non-point sources, such as organic and inorganic fertilizers, have been increasingly recognized as a major contributor to N pollution in catchments (Dupas et al., 2015). In many karst catchments worldwide, N fertilizer is a major contributor to aquifer contamination (Panno et al., 2001; Minet et al., 2017; Eller and Katz, 2017). In

southwest China, one of the largest continuous karst areas in the world, researchers also identified agricultural activities as the predominant source of aquifer N, but found the contribution of atmospheric N to be negligible (Yang et al., 2013). Consequently, spatially and temporally targeted fertilization management is becoming more important for effective, catchment-wide reductions in N loss from land to water. The simulated N fluxes showed that the proportion of N uptake by crops was no >50% of the fertilizer applied, which means there are marked N losses and/or accumulation in the karst system. Therefore, improving the efficiency of fertilization represents a priority for reducing the N losses and subsequent contamination of water. In addition, the main period of fertilizer application is usually in May in the study area (Yue et al., 2019), corresponding to the end of the dry season and beginning of the rainy season. Consequently, applied N will rapidly infiltrate to the deeper soil layers, the epikarst, and even the deep flow zone during heavy rainfall events leading to the N loss. Importantly when water levels in sub-surface conduits increase beyond sustaining the low flows from the karst aquifer, the water will flow into small fractures from conduits (Zhang et al., 2017b). Consequently, N transported will also enter the small fractures and accumulate, leading to extensive, potentially long-term contamination of the karst system. Elsewhere the karst system has been observed to delay N flux to streams during storm events and thereafter export N at a more gradual rate distributed over the flood recession (Husic et al., 2019). To reduce the N loss and karst critical zone pollution (mainly in the epikarst), measures to reduce the N entering the underground system are critical for mitigating epikarst N loading, such as decreasing the N input during periods when there is strong hydraulic connectivity between soil and epikarst/deep flow zone. Therefore, fertilization may be more reasonable if timed for drier periods before the wet season starts or large storm events are forecast.

N management scenarios within karst catchments should not only consider the N fluxes within the surface or underground system but also the transformation of N between them via the sinkholes. Since a large number of sinkholes are located in the cultivated land of plain and valley areas, restricting fertilization around sinkholes to decrease the concentrated and fast loss of N is necessary for spatial zoning of agricultural activities.

6. Conclusions

Water and N transport in karst areas depend strongly on the structure of the critical zone and the karst flow system. In this study, a hydrological-biogeochemical model was developed by considering the effects of unique karstic characteristics on flow and N dynamics.

The model has been successfully applied in the karst catchment of Houzhai where detailed observation data of flow, stable isotopes and N concentrations, and geomorphological surveys for soil properties, fracture distribution and karst topography were available. Uncertainty analysis using Monte Carlo analysis and multi-objective calibration was used targeting initially flow and water stable isotopes, and then N simulations. Multiple sources of observations are used to identify main controlling factors of N loading, such as hydrological dynamics in the catchment. The multi-objective calibration, combining discharge with water stable isotopes, can significantly constrain the parameters and reduce equifinality effect of parameters on the simulated results. The modelling results reveal functional effects of karst geomorphology and land use on spatio-temporal variations of hydrological processes and N transport, such as the large amount of N released from soil reservoirs to the epikarst (via fractures or sinkholes) and then exported to the underground channel. The modelling results also show regional differences of hydrological processes and N transport in relation to the distribution of soils, epikarst and groundwater aquifer controlled by geological conditions. In the limestone area of the south characterized by the thin soils, rich fractures and sinkholes, the flow and NO_3-N loadings in the underground channel are about 2.3 and 2 times larger,

respectively, than those in the north surface stream overlying the dolomite stone.

The large proportion of N draining into groundwater could lead to extensive, potentially long-term contamination of the karst system. Therefore, improving the efficiency of fertilization is an urgent need to reduce the N losses and contamination. It is worth noting that in karst landscapes with surrounding hills separated by star-shaped valleys, in the southwest of China, most sinkholes are distributed in the valleys covered by thick soil. These areas are often characterized by farmland, with high N inputs due to fertilizer applications. Therefore, improving agricultural management in valleys/depressions has a key role to play in reducing regional N loss and pollution in karst area.

The modelling indicates that uncertainty increases with model complexity and parameterisation. Strengthening the modelling capability particularly biogeochemical processes, is vital for understanding transport of N and other N components. Improvements to the modelling could be achieved if supported by additional surveys of geological conditions to describe the strong heterogeneity of the karst structure in detail, and biogeochemical analysis, such as ^{15}N-NO$_3$, to trace N sources and its transformation. Importantly, in addition to input-output observations, monitoring of hydrological and biogeochemical dynamics in different zones, such as vegetation, soils, epikarst and deep aquifer, can help adequate expressions of hydrological and biogeochemical processes in each medium and further improve the reliability of the modelling results.

CRediT authorship contribution statement

Zhicai Zhang: Conceptualization, Methodology, Software, Writing - original draft. **Xi Chen:** Conceptualization, Writing - review & editing, Supervision. **Qinbo Cheng:** Investigation, Data curation. **Siliang Li:** Validation, Conceptualization. **Fujun Yue:** Data curation, Resources. **Tao Peng:** Data curation, Resources. **Susan Waldron:** Writing - review & editing, Visualization. **David Oliver:** Writing - review & editing, Visualization. **Chris Soulsby:** Writing - review & editing, Supervision.

Declaration of competing interest

The authors declare that they have no known competing financial interests or personal relationships that could have appeared to influence the work reported in this paper.

Acknowledgments

References

Arnold, J.G., Srinivasan, R., Muttiah, R.S., Williams, J.R., 1998. Large area hydrologic modeling and assessment part I: model development. J. Am. Water Resour. Assoc. 34, 73–89.

Barton, L., McLay, C.D.A., Schipper, L.A., Smith, C.T., 1999. Annual denitrification rates in agricultural and forest soils: a review. Aust. J. Soil Res. 37 (6), 1073–1093.

Bicknell, B.R., Imhoff, J.C., Kittle, J.L., Donigian, A.S., Johanson, R.C., 1993. Hydrological Simulation Program-Fortran (HSPF): User's Manual for Release 10.0. EPA-600/3-84-066. Environmental Research Laboratory, USEPA, Athens, GA.

Binkley, D., Cromack Jr., K., Baker, D., 1994. Nitrogen fixation by red alder: biology, rates, and controls. In: Hibbs, D. (Ed.), The Biology and Management of Red Alder. Oregon State University Press, Corvallis, pp. 57–72.

Birkel, C., Soulsby, C., Tetzlaff, D., 2015. Conceptual modelling to assess how the interplay of hydrological connectivity, catchment storage and tracer dynamics controls nonstationary water age estimates. Hydrol. Process. 29, 2956–2969.

Bosch, N.S., Allan, J.D., 2008. The influence of impoundments on nutrient budgets in two catchments of Southeastern Michigan. Biogeochemistry 87 (3), 325–338.

Brooks, R.H., Corey, A.T., 1964. Hydraulic properties of porous media, hydrology papers, Colorado State University. Pap. 3. Fort Collins CO. https://doi:citeulike-article-id: 711012.

Chen, X., Chen, C., Hao, Q., Zhang, Z., Shi, P., 2008. Simulation of rainfall-underground outflow responses of a karstic watershed in Southwest China with an artificial neural network. Sinkholes and the Engineering and Environmental Impacts of Karst. American Society of Civil Engineers, Reston, VA, pp. 433–443.

Chen, X., Zhang, Z., Soulsby, C., Cheng, Q., Binley, A., Jiang, R., Tao, M., 2018. Characterizing the heterogeneity of karst critical zone and its hydrological function: an integrated approach. Hydrol. Process. 32, 2932–2946.

Cheng, Q., 2008. Perspectives in biological nitrogen fixation research. J. Integr. Plant Biol. 50, 786–798.

Cheng, Q., Chen, Xi, Chen, Xunhong, Zhang, Z., Ling, M., 2011. Water infiltration underneath single-ring permeameters and hydraulic conductivity determination. J. Hydrol. 398, 135–143.

David, M.B., Wall, L.G., Royer, T.V., Tank, J.L., 2006. Denitrification and the nitrogen budget of a reservoir in an agricultural landscape. Ecol. Appl. 16 (6), 2177–2190.

Dupas, R., Delmas, M., Dorioz, J.-M., Garnier, J., Moatar, F., Gascuel-Odoux, C., 2015. Assessing the impact of agricultural pressures on N and P loads and eutrophication risk. Ecol. Indic. 48, 396–407.

Eller, K.T., Katz, B.G., 2017. Nitrogen source inventory and loading tool: an integrated approach toward restoration of water-quality impaired karst springs. J. Environ. Manag. 196, 702–709.

Ferrant, S., Oehler, F., Durand, P., Ruiz, L., Salmon-Monviola, J., Justes, E., Dugast, P., Probst, A., Probst, J.-L., Sanchez-Perez, J.-M., 2011. Understanding nitrogen transfer dynamics in a small agricultural catchment: comparison of a distributed (TNT2) and a semi distributed (SWAT) modeling approaches. J. Hydrol. 406, 1–15.

Ford, D.C., Williams, P.W., 1989. Karst Geomorphology and Hydrology. Unwin Hyman, London.

Godwin, D.C., Jones, C.A., Ritchie, J.T., Vlek, P.L.G., Youngdahl, L.J., 1984. The water and nitrogen components of the CERES models. Proc. Int. Symp. Minim. Data Sets Agrotechnology Transf. Patancheru, India.

Han, Z.W., Zhang, S., Wu, P., Cao, X.X., Tu, H., 2017. Distribution characteristics of nitrogen and phosphorus in waters and release flux estimation in the sediment of Caohai basin, Guizhou. Chinese Journal of Ecology 36 (9), 2501–2506.

Hartmann, A., Goldscheider, N., Wagener, T., Lange, J., Weiler, M., 2014. Karst water resources in a changing world: review of hydrological modeling approaches. Rev. Geophys. 52, 218–242.

Heathwaite, A.L., Quinn, P.F., Hewett, C.J.M., 2005. Modelling and managing critical source areas of diffuse pollution from agricultural land using flow connectivity simulation. J. Hydrol. 304, 446–461.

Hénault, C., Germon, J.C., 2000. NEMIS, a predictive model of denitrification on the field scale. Eur. J. Soil Sci. 51, 257–270.

Hu, M., Liu, Y., Wang, J., Dahlgren, R.A., Chen, D., 2018. A modification of the Regional Nutrient Management model (ReNuMa) to identify long-term changes in riverine nitrogen sources. J. Hydrol. 561, 31–42.

Husic, A., Fox, J., Adams, E., Ford, W., Agouridis, C., Currens, J., Backus, J., 2019. Nitrate pathways, processes, and timing in an agricultural karst system: development and application of a numerical model. Water Resour. Res. 55, 2079–2103.

Inamdar, S.P., Lowrance, R.R., Altier, L.S., Williams, R.G., Hubbard, R.K., 1999. Riparian Ecosystem Management Model (REMM): II. Testing of the water quality and nutrient cycling component for a coastal plain riparian system. Transactions of the ASAE 42 (6), 1691–1707.

Jarvie, H.P., Withers, P.J.A., Hodgkinson, R., Bates, A., Neal, M., Wickham, H.D., Harman, S.A., Armstrong, L., 2008. Influence of rural land use on streamwater nutrients and their ecological significance. J. Hydrol. 350, 166–186.

Jarvie, H.P., Johnson, L.T., Sharpley, A.N., Smith, D.R., Baker, D.B., Bruulsema, T.W., Confesor, R., 2017. Increased soluble phosphorus loads to Lake Erie: unintended consequences of conservation practices? J. Environ. Qual. 46, 123–132.

Jones, A.L., Smart, P.L., 2005. Spatial and temporal changes in the structure of groundwater nitrate concentration time series (1935–1999) as demonstrated by autoregressive modelling. J. Hydrol. 310, 201–215.

Kelleher, C., Wagener, T., McGlynn, B., 2015. Model-based analysis of the influence of catchment properties on hydrologic partitioning across five mountain headwater subcatchments. Water Resour. Res. 51, 4109–4136.

Klimchouk, A., 2004. Towards defining, delimiting and classifying epikarst: its origin, processes and variants of geomorphic evolution. Speleogenes. Evol. Karst Aquifers. 2 (1), 1–13.

Kling, H., Fuchs, M., Paulin, M., 2012. Runoff conditions in the upper Danube basin under an ensemble of climate change scenarios. J. Hydrol. 424–425, 264–277.

Kovacs, A., Honti, M., Zessner, M., Eder, A., Clement, A., Blöschl, G., 2012. Identification of phosphorus emission hotspots in agricultural catchments. Sci. Total Environ. 433, 74–88.

Kruse, S., Grasmueck, M., Weiss, M., Viggiano, D., 2006. Sinkhole structure imaging in covered karst terrain. Geophys. Res. Lett. 33, L16405.

Li, C., Aber, J., Stange, F., Butterbach-Bahl, K., Papen, H., 2000. A process-oriented model of N$_2$O and NO emissions from forest soils: 1. Model development. J. Geophys. Res. Atmos. 105, 4369–4384.

Li, C., Li, S.L., Yue, F.J., Liu, J., Zhong, J., Yan, Z.F., Zhang, R.C., Wang, Z.J., Xu, S., 2019. Identification of sources and transformations of nitrate in the Xijiang River using nitrate isotopes and Bayesian model. Sci. Total Environ. 646, 801–810.

Liu, C.Q., 2009. Biogeochemical Processes and Cycling of Nutrients in the Earth's Surface: Cycling of Nutrients in Soil–Plant Systems of Karstic Environments, Southwest China. (In Chinese). Science Press, Beijing, China.

Mahler, B.J., Garner, B.D., 2009. Using nitrate to quantify quick flow in a karst aquifer. Ground Water 47 (3), 350–360.

McDonnell, J.J., Beven, K., 2014. Debates - the future of hydrological sciences: a (common) path forward? A call to action aimed at understanding velocities, celerities and residence time distributions of the headwater hydrograph. Water Resour. Res. 50, 5342–5350.

Minet, E.P., Goodhue, R., Meier-Augenstein, W., Kalin, R.M., Fenton, O., Richards, K.G., Coxon, C.E., 2017. Combining stable isotopes with contamination indicators: a method for improved investigation of nitrate sources and dynamics in aquifers with mixed nitrogen inputs. Water Res. 124, 85–96.

Opsahl, S.P., Musgrove, M., Slattery, R.N., 2017. New insights into nitrate dynamics in a karst groundwater system gained from in situ high-frequency optical sensor measurements. J. Hydrol. 546, 179–188.

Panno, S., Hackley, K., Hwang, H., Kelly, W., 2001. Determination of the sources of nitrate contamination in karst springs using isotopic and chemical indicators. Chem. Geol. 179, 113–128.

Perrin, J., Jeannin, P.-Y., Zwahlen, F., 2003. Epikarst storage in a karst aquifer: a conceptual model based on isotopic data, Milandre test site, Switzerland. J. Hydrol. 279, 106–124.

Perrin, J., Jeannin, P.Y., Cornaton, F., 2007. The role of tributary mixing in chemical variations at a karst spring, Milandre, Switzerland. J. Hydrol. 332, 152–173.

Pi, F., 2017. Study on Forest Ecological Stoichiometry and Carbon, Nitrogen and Phosphorus Cycle in Karst Region of Central Guizhou. Guizhou University (Master's thesis; in Chinese).

Pionke, H.B., Gburek, W.J., Sharpley, A.N., Schnabel, R.R., 1996. Flow and nutrient export patterns for an agricultural hill-land watershed. Water Resour. Res. 32, 1795–1804.

Piovano, T.I., Tetzlaff, D., Ala-aho, P., Buttle, J., Mitchell, C.P.J., Soulsby, C., 2018. Testing a spatially distributed tracer-aided runoff model in a snow-influenced catchment: effects of multicriteria calibration on streamwater ages. Hydrol. Process. 32, 3089–3107.

Powers, S.M., Tank, J.L., Robertson, D.M., 2015. Control of nitrogen and phosphorus transport by reservoirs in agricultural landscapes. Biogeochemistry 124 (1–3), 417–439.

Ranzini, M., Forti, M.C., Whitehead, P.G., Arcova, F.C.S., de Cicco, V., Wade, A.J., 2007. Integrated Nitrogen CAtchment model (INCA) applied to a tropical catchment in the Atlantic Forest, São Paulo, Brazil. Hydrol. Earth Syst. Sci. 11, 614–622.

Reddy, K.R., Khaleel, R., Overcash, M.R., Westerman, P.W., 1979. A nonpoint source model for land areas receiving animal wastes: I. Mineralization of organic nitrogen. Trans. ASAE 22, 0863–0872.

Sanford, W.E., Pope, J.P., 2013. Quantifying groundwater's role in delaying improvements to Chesapeake Bay water quality. Environ. Sci. Technol. 47, 13330–13338.

Saunders, D.L., Kalff, J., 2001. Nitrogen retention in wetlands, lakes and rivers. Hydrobiologia. 443 (1/3), 205–212.

Schaefli, B., Gupta, H.V., 2007. Do Nash values have value? Hydrol. Process. 21, 2075–2080.

Shaughnessy, A.R., Sloan, J.J., Corcoran, M.J., Hasenmueller, E.A., 2019. Sediments in agricultural reservoirs act as sinks and sources for nutrients over various timescales. Water Resour. Res. 55, 5985–6000.

Smil, V., 1999. Nitrogen in crop production: an account of global flows. Glob. Biogeochem. Cycles 13, 647–662.

Soulsby, C., Birkel, C., Geris, J., Dick, J., Tunaley, C., Tetzlaff, D., 2015. Stream water age distributions controlled by storage dynamics and nonlinear hydrologic connectivity: modeling with high-resolution isotope data. Water Resour. Res. 51, 7759–7776.

Sprenger, M., Volkmann, T.H.M., Blume, T., Weiler, M., 2015. Estimating flow and transport parameters in the unsaturated zone with pore water stable isotopes. Hydrol. Earth Syst. Sci. 19, 2617–2635.

Thanapakpawin, P., 2007. Spatially-distributed Modeling of Hydrology and Nitrogen Export From Watersheds. PHD's thesis. University of Washington.

Thyer, M., Beckers, J., Spittlehouse, D., Alila, Y., Winkler, R., 2004. Diagnosing a distributed hydrologic model for two high-elevation forested catchments based on detailed stand- and basin-scale data. Water Resour. Res. 40.

Tihansky, A.B., 1999. Sinkholes, west-central Florida: A link between surface water and ground water, in Galloway, D., Jones, D.R., and Ingebritsen, S.E., eds.,. L. Subsid. United States US Geol. Surv. Circ. 1182, 121–140.

Wang, Z.J., Li, S.L., Yue, F.J., Qin, C.Q., Buckerfield, S., Zeng, J., 2020. Rainfall driven nitrate transport in agricultural karst surface river system: insight from high resolution hydrochemistry and nitrate isotopes. Agric. Ecosyst. Environ. 291, 106787.

Wigmosta, M.S., Perkins, W.A., 2001. Simulating the effects of forest roads on watershed hydrology. In: Wigmosta, M., Burgess, S. (Eds.), Land Use and Watersheds: Human Influence on Hydrology and Geomorphology in Urban and Forest Areas, Water Sci. Appl. Ser. vol. 2. AGU, Washington, D. C, pp. 127–143.

Wigmosta, M.S., Vail, L.W., Lettenmaier, D.P., 1994. A distributed hydrology-vegetation model for complex terrain. Water Resour. Res. 30, 1665–1679.

Williams, P.W., 2008. The role of the epikarst in karst and cave hydrogeology: a review. Int. J. Speleol. 37 (1), 1–10.

Xie, Y., Cook, P.G., Simmons, C.T., Partington, D., Crosbie, R., Batelaan, O., 2018. Uncertainty of groundwater recharge estimated from a water and energy balance model. J. Hydrol. 561, 1081–1093.

Yang, Y., 2001. A study on the structure of karst aquifer medium and the groundwater flow in Houzhai underground river basin. Carsologica Sinica 20 (1) (In Chinese).

Yang, P., Yuan, D., Ye, X., Xie, S., Chen, X., Liu, Z., 2013. Sources and migration path of chemical compositions in a karst groundwater system during rainfall events. Chin. Sci. Bull. 58, 2488–2496.

Yao, C.Q., 2006. Simulation of Watershed Land-surface Hydrological Process and its Integration With GIS. PHD's thesis. Beijing Normal University (in Chinese).

Yao, F., Sun, J., Tang, C., Ni, W., 2011. Kinetics of ammonium, nitrate and phosphate uptake by candidate plants used in constructed wetlands. Procedia Environ. Sci. 10, 1854–1861.

Yu, J.B., Yang, L.Z., Zhang, H.S., Fang, M.Z., Xing, F.M., 1990. The Study of Development Regularity of Karst in China - Water Resources Evaluation and Exploitation in Karst Region in South of Puding in Guizhou Province. Science Press of China (In Chinese).

Yue, F.J., Li, S.L., Liu, C.Q., Lang, Y.C., Ding, H., 2015. Sources and transport of nitrate constrained by the isotopic technique in a karst catchment: an example from Southwest China. Hydrol. Process. 29, 1883–1893.

Yue, F.-J., Waldron, S., Li, S.-L., Wang, Z.-J., Zeng, J., Xu, S., Zhang, Z.-C., Oliver, D.M., 2019. Land use interacts with changes in catchment hydrology to generate chronic nitrate pollution in karst waters and strong seasonality in excess nitrate export. Sci. Total Environ. 696, 134062.

Zeng, J., 2018. Chemical Characterization of Rainwater and Spatial-temporal Variation of Nitrogen Deposition in a Small Karst Catchment. Master's thesis. Guizhou University (in Chinese).

Zhang, Y., Shao, Q., 2018. Uncertainty and its propagation estimation for an integrated water system model: an experiment from water quantity to quality simulations. J. Hydrol. 565, 623–635.

Zhang, Z., Chen, X., Ghadouani, A., Shi, P., 2011. Modelling hydrological processes influenced by soil, rock and vegetation in a small karst basin of southwest China. Hydrol. Process. 25, 2456–2470.

Zhang, Z.C., Chen, X., Liu, J.T., Peng, T., Shi, P., Yan, X.L., 2012. Influence of terrain on epikarst in karst mountain - a case study of Chenqi catchment. Earth and environment 40 (2), 137–143 (In Chinese).

Zhang, Z., Chen, Xi, Chen, Xunhong, Shi, P., 2013. Quantifying time lag of epikarst-spring hydrograph response to rainfall using correlation and spectral analyses. Hydrogeol. J. 21, 1619–1631.

Zhang, Y.Y., Shao, Q.X., Ye, A.Z., Xing, H.T., Xia, J., 2016. Integrated water system simulation by considering hydrological and biogeochemical processes: model development, with parameter sensitivity and autocalibration. Hydrol. Earth Syst. Sci. 20, 529–553.

Zhang, Y., Gao, Y., Yu, Q., 2017a. Diffuse nitrogen loss simulation and impact assessment of stereoscopic agriculture pattern by integrated water system model and consideration of multiple existence forms. J. Hydrol. 552, 660–673.

Zhang, Z., Chen, X., Soulsby, C., 2017b. Catchment-scale conceptual modelling of water and solute transport in the dual flow system of the karst critical zone. Hydrol. Process. 31, 3421–3436.

Zhang, W., Li, Y., Zhu, B., Zheng, X., Liu, C., Tang, J., Su, F., Zhang, C., Ju, X., Deng, J., 2018. A process-oriented hydro-biogeochemical model enabling simulation of gaseous carbon and nitrogen emissions and hydrologic nitrogen losses from a subtropical catchment. Sci. Total Environ. 616–617, 305–317.

Zhang, Z., Chen, X., Cheng, Q., Soulsby, C., 2019. Storage dynamics, hydrological connectivity and flux ages in a karst catchment: conceptual modelling using stable isotopes. Hydrol. Earth Syst. Sci. 23, 51–71.